In situ growth of Bi/Ag double quantum dots on hollow Bi_2MoO_6 microspheres: Enhancement of the surface plasmon resonance effect on PMS activation

Yao Deng [a], Juntao Wang [b], Jing Wang [c], Huidi Zhang [c], Hongbo Xiao [a,d], Cuihong Zhang [d], Wenlei Wang [a,d,*]

[a] College of Science, Central South University of Forestry and Technology, Changsha 410004, China
[b] School of Nuclear Technology and Chemistry & Biology, Hubei University of Science and Technology, Xianning 437100, China
[c] College of Materials Science and Engineering, Central South University of Forestry and Technology, Changsha 410004, China
[d] Institute of Chemical Disposal and Resource Utilization of Hazardous Wastes, Central South University of Forestry and Technology, Changsha 410004, China

ARTICLE INFO

ABSTRACT

In this work, the effect of Bi/Ag double quantum dots on plasmon resonance and PMS activation was investigated. Bi/Ag double quantum dots were generated in situ on hollow Bi_2MoO_6 microspheres by stepwise irradiation using a high-energy β electron beam. The formation of Bi/Ag DQDs greatly optimized the drawbacks of Bi_2MoO_6 in terms of light absorption. Synergistic introduction of DQDs greatly reduced the band gap from 2.72 eV to 2.12 eV. The $Bi-Ag@Bi_2MoO_6 - 400/PMS$ system degraded ciprofloxacin with kinetic constants 10 and 12 times higher than those of the $Bi@Bi_2MoO_6/PMS$ and Bi_2MoO_6/PMS systems. The formation of an electron transfer path from Ag QDs to Bi QDs enhanced the SPR effect of Bi QDs. $\cdot O_2^-$ and $^1O_2$ played a major role in the CIP degradation process. This study will provide a new strategy for enhancing the Bi plasmon resonance effect and provide a technical method to the efficient degradation of antibiotics in water.

1. Introduction

Water pollution has become a serious environmental problem in today's world. Among the various causes of water pollution, the pollution caused by the abuse of antibiotics in the medical industry, livestock breeding and agricultural production has become a major challenge to global health and has aroused widespread attention from researchers [1–3]. Ciprofloxacin is a very common third-generation fluoroquinolone antibiotic that belongs to a broad spectrum of antibacterial active drugs and a relatively wide range of drugs. However, more than 75% of ciprofloxacin cannot be metabolized in vivo, and inefficient removal at wastewater treatment plants results in the continued discharge of ciprofloxacin into the aquatic environment. Therefore, it is of practical significance to propose appropriate and effective ciprofloxacin removal strategies to reduce the degree of water pollution [4]. Researchers have used different methods to degrade ciprofloxacin-containing wastewater, such as ozonation [5], advanced oxidation processes [6], activated carbon and talc [7], adsorption of surface-modified carbon materials and various other methods [8].

In recent decades, advanced oxidation processes have received much attention from researchers because of their good degradation of refractory organic pollutants in wastewater, especially those based on highly reactive sulfate radicals (SR−AOPs) [9]. The coexistence of sulfate radicals ($\cdot SO_4^-$, $E^\theta = 2.5 -3.1$ V vs. NHE) and hydroxyl radicals ($\cdot OH$, $E^\theta = 1.8 -2.7$ V vs. NHE) in SR−AOPs results in higher oxidation selectivity and pH-independent reactivity than in AOPs with only hydroxyl radicals [10]. Peroxymonosulfate and peroxonodisulfate are representative oxidants that start the reaction process. Peroxymonosulfate is easier to activate because of the asymmetry of its structure ($HO-SO_4^-$), which facilitates the breakage of the O−O bond to form $\cdot SO_4^-$ and $\cdot OH$ [11]. To date, many activation methods, including ultrasound, UV, heating, transition metals, and metal-free materials (graphene, carbon nanotubes, reduced graphene oxide, and activated carbon), have been used to activate PMS [12,13]. However, physical activation of PMS, such as heating, ultrasound and UV irradiation, is very dependent on a large amount of energy supply and has very low social benefits, so they are not ideal strategies. Secondary pollution caused by transition metal ions and metal oxides has limited their

development in AOPs [14]. Thus, finding more economical and efficient ways to activate PMS is very important.

Photocatalyst-based photoactivation technology is recognized as a low-carbon method of PMS activation credited to its excellent photo-initiation and environmental friendliness. In the literature, the addition and activation of PMS during photocatalysis is one of the many ways to promote the effect of photocatalysis. PMS can enhance the photocatalytic performance because it can act as an electron acceptor and be activated to produce sulfate radicals by accepting photogenerated electrons [15]. Therefore, semiconductors are widely used as activators for PMS activation. In recent years, Bi-based materials, especially Bi quantum dots (QDs), due to their low cost, excellent electronic conductivity, small particle size and surface plasmon resonance effect (SPR), have been used to induce the formation of hot electrons and hot holes [16]. Bi quantum dots can also act as electron traps to trap photogenerated electrons and inhibit the compounding of photogenerated electrons with holes, thus emerging as a potential catalyst for SR−AOP applications [17]. Nevertheless, the low chemical stability of bismuth metal affects its wide application. Researchers have reported some bismuth-based composites, such as the preparation of bismuth nanosphere monodisperse graphene oxide as plasma photocatalysts to remove NO under ultraviolet irradiation [18]. In addition, the antibacterial activity of bismuth nanospheres/graphene nanocomposites was reinforced by coupling Bi metals to graphene [19]. However, due to the weak strength of the SPR effect on Bi itself, the enhancement of the catalytic effect of the reaction system is hardly comparable to that of plasma metals such as gold, silver and copper. The SPR effect of Bi was not enhanced in the current study. Among various plasma metals, silver has attracted much attention due to its excellent SPR characteristics and good catalytic activity for various chemical reactions [20]. However, the plasmon formant of Ag nanospheres is in the near ultraviolet region of the solar spectrum, which does not match the solar spectrum, limiting their application in solar-driven photocatalysis [21]. In addition, Ag is easily oxidized under natural environmental conditions, which leads to the weakening of the plasma effect [22]. At the same time, precious metals are not suitable for commercial application in photocatalysis from the perspective of economic cost due to their rare sources. According to previous studies [23,24], a hypothesis is proposed: coupling a small amount Ag quantum dots with Bi quantum dots will enhance the SPR effect of Bi quantum dots, while silver as a transition metal can lead to complete activation of PMS and efficient degradation of CIP. Ag also has good stability by controlling the direction of electron migration and avoiding the oxidation of Ag quantum dots.

The purpose of this study is to explore the enhancement of the SPR effect of Ag quantum dots on Bi quantum dots and its effect on photocatalytic activity. Bi_2MoO_6 nanospheres with hollow core-shells were prepared by a one-pot template-free method and used as model materials to induce in situ generation of Bi quantum dots by β particle irradiation. At the same time, a AgI/Bi_2MoO_6 composite material was prepared, and in situ formation of Bi−Ag double quantum dots was induced by β particle irradiation. Double quantum dot formation was verified by transmission electron microscopy. The effects of double quantum dots on the material and the photocatalytic properties were analyzed by UV−vis DRS, Mott-Schottky, and VB-XPS from the perspective of light absorption and energy band. The effect of Ag quantum dots on the charge density distribution of Bi quantum dots and their composites was investigated by using density flooding theory (DFT). The main effective components in different systems of photocatalysts were examined by electron paramagnetic resonance spectroscopy (EPR) and free radical quenching experiments. Furthermore, the effects of PMS concentration, dissolved oxygen content and pH on different free radicals were further investigated. The hypothesis that Ag enhances the Bi SPR effect is verified, which provides a feasible method for practical application of the Bi SPR effect.

2. Experimental section

2.1. Chemicals

Bismuth nitrate pentahydrate (Bi(NO)₃·5 H₂O), sodium molybdate dihydrate (Na_2MoO_6·2 H₂O), silver nitrate (AgNO₃), potassium iodide (KI), ciprofloxacin (CIP), PMS (KHSO₅·0.5KHSO₄·0.5 K₂SO₄), methanol (MeOH), tert-butanol (TBA), benzoquinone (BQ), disodium ethylenediamine tetraacetate (EDTA-2Na), dimethyl sulfoxide (DMSO), L-histidine (His) and ethylene glycol (EG, (CH₂OH)₂) were sourced from Sinopharm Chemical Reagent Company (Shanghai, China).

2.2. Synthesis of photocatalysts

2.2.1. Preparation of Bi_2MoO_6 hollow microspheres

Bi(NO)₃·5 H₂O (0.2 mmol) was dissolved in 8.00 mL glycol for 1 h, and 10 mmol Na_2MoO_6·2 H₂O was dissolved in 8.00 mL glycol for 1 h. Then, the mixture was poured into 40.00 mL isopropyl alcohol. Finally, the mixture was transferred to a 100.00 mL Teflon-lined stainless steel autoclave. The autoclave was sealed and kept at 160 ℃ for 24 h. The white sediment was then collected and repeatedly cleaned with deionized water and ethanol and finally dried at 60 ℃ for 12 h.

2.2.2. Preparation of AgI/Bi_2MoO_6 composites

Bi_2MoO_6 (0.3000 g) was added to 50.00 mL deionized water for 15 min of ultrasonic dispersion, and then a certain amount of AgNO₃ ultrasonic dispersion was added for 15 min of ultrasound and stirred for 1 h. Then, KI with the same molar ratio was added to the solution and stirred for another 1 h. The solution was collected and cleaned repeatedly with deionized water and ethanol. Finally, it was dried at 60 ℃ for 10 h.

2.2.3. Preparation of $Bi−Ag@AgI/Bi_2MoO_6$ composites

AgI/Bi_2MoO_6 composites were dispersed in 60 * 80 mm films at room temperature and prepared by irradiation with different doses of electron beams with a 1 MeV electron accelerator (Wasik Associates, USA). Irradiation was performed with a voltage of 1000 KeV, a beam current of 20 mA, and a dose rate of 20 KGy (1 Gy = 1 J/kg) (range, 20 −240 KGy). AgI/Bi_2MoO_6 was modified with high-energy beta particles at doses of 200, 400, 600, and 800 Kgy. The final samples obtained were named $Bi−Ag@Bi_2MoO_6$ − 200, $Bi−Ag@Bi_2MoO_6$ − 400, $Bi−Ag@Bi_2MoO_6$ − 600, and $Bi−Ag@Bi_2MoO_6$ − 800.

2.3. Characterizations

The morphology and microstructure of the photocatalyst were obtained by scanning electron microscopy (SEM, SIGMA 300, ZEISS, Germany). The microstructure of all samples was studied by transmission electron microscopy (TEM, FEI Tecnai G20, Tecnai, USA). UV−vis DRS were recorded for all samples using a UV—vis spectrophotometer (UV−vis, UV-3600, Shimazu, Japan) based on BaSO₄. Photoluminescence spectra were measured using a fluorescence spectrophotometer (PL, FLS1000, Edinburgh, UK). The photocatalyzed crystal phases were identified by powder X-ray diffraction (XRD, D8 Advance, Bruke) with Cu Kα radiation and a scanning speed of 3° min⁻¹. Raman diffraction (Raman, Horiba LabRAM HR Evolution, Japan) was used to study the properties and structures of the photocatalysts. Fourier transform infrared spectroscopy (FT-IR) of samples in KBr pellets was recorded on a Thermo Scientific iN10 with a scanning range of 400 cm⁻¹ to 4000 cm⁻¹. XPS (KRATOS, Shimadzu, Japan) was used to measure the chemical state and relative content of each element in the material. Electrochemical impedance spectra and transient photocurrent responses were measured on an electrochemical workstation (CHI 660e, CHI Shanghai) using a three-electrode system. Mott-Schottky plots were prepared at 1000 Hz by using the electrochemical workstation and AgCl as the reference electrode. The active substances in the photocatalytic

process were analyzed by paramagnetic resonance spectroscopy (Bruker EMXplus-6/1, Germany).

### 2.4. Experimental process of photocatalysis

The photocatalytic performance of CIP degradation by the photocatalyst was studied with CIP as the target pollutant in a photochemical reaction instrument, which was purchased from Shanghai Yuncao Electronic Technology Co. The photocatalytic instrument consists of a light source with 300 W xenon lamp, a magnetic stirrer, a light source controller, a reaction dark box and a cooling water circulation device. The size of quartz test tube is 50 mL and the thickness is 2 mm. The adsorption and photocatalysis were carried out by adding 20.0 mg photocatalyst into 40.0 mL CIP hydrochloric acid solution with a concentration of 10 mg/L. The reaction system reached adsorption-desorption equilibrium by stirring in the dark for 30 min. After stirring for 30 min, the light source was turned on. A 300 W xenon lamp was used as the light source for the photocatalytic reaction ($\lambda \geq 420$ nm). After a certain interval of time, 2.0 mL of the reaction solution was extracted from the suspension using a syringe with a 0.45 μm filter. Determination of CIP concentration by high-performance liquid chromatography. Under the same conditions, PMS was introduced for a control test to verify the activation effect of the photocatalyst on PMS. Cyclic experiments were performed under the same experimental conditions. The intermediate product in the photocatalytic degradation of CIP was determined by high-performance liquid chromatography—mass spectrometry. The pH values of different photocatalyst systems were adjusted by hydrochloric acid and sodium hydroxide solutions. The influence of oxygen concentration on the reaction was explored by changing the concentration of dissolved oxygen by adjusting the introduced concentration of O_2 and N_2.

3. Results and discussion

3.1. Characterization of the prepared catalyst

The synthetic process of Bi−Ag@BMO− β is shown in Fig. 1a. The AI/BMO photocatalyst was synthesized from a two−step reaction.
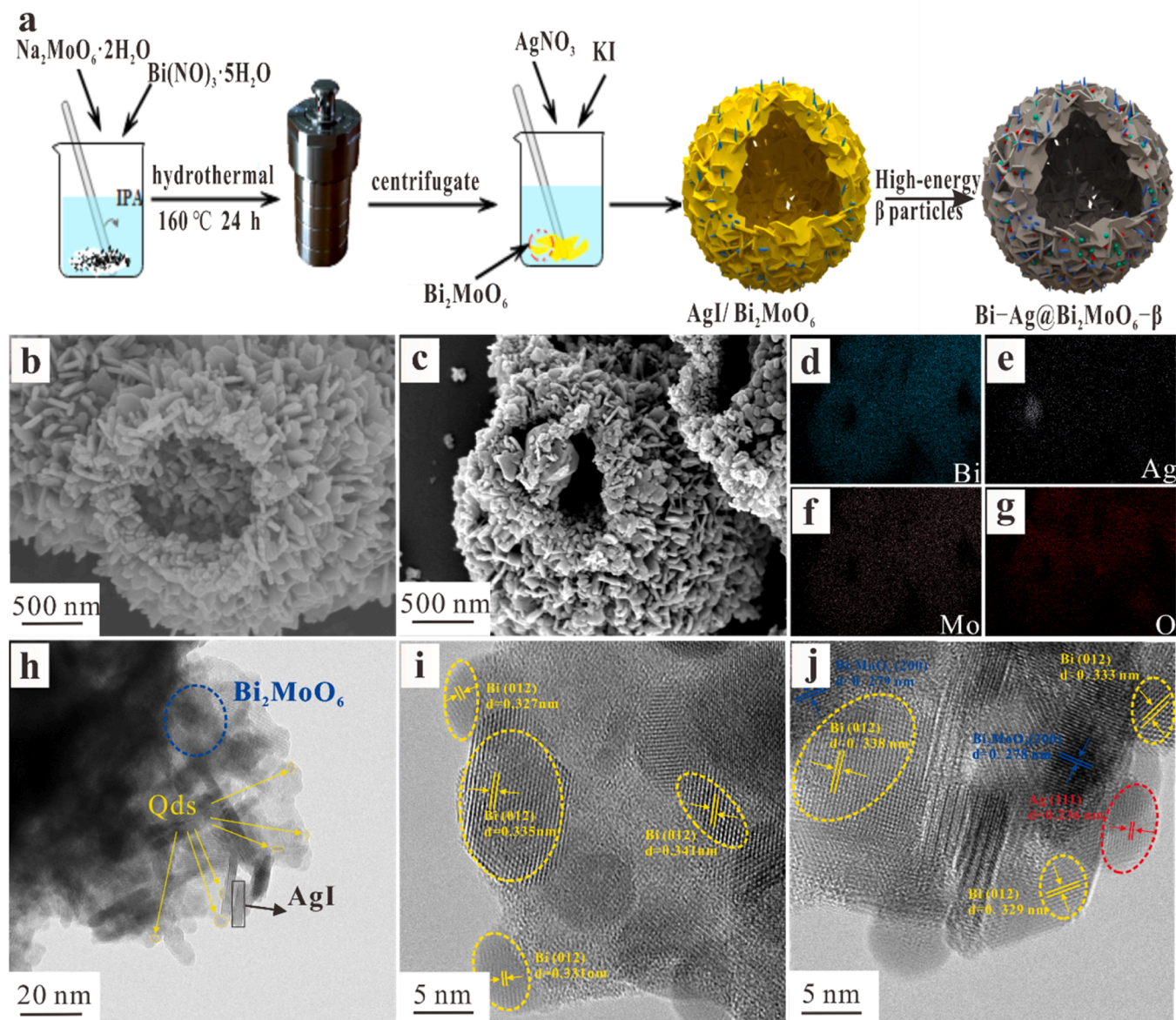
Fig. 1. (a) Schematic illustration of the preparation processes of Bi−Ag@BMO− β. SEM micrographs of (b) BMO. (c) Bi−Ag@BMO− 400. (d−g) EDS mapping of Bi−Ag@BMO− 400. (h) TEM micrographs of Bi−Ag@BMO− 400. (i − j) HRTEM micrographs of Bi−Ag@BMO− 400.

Consequently, Bi−Ag double quantum dots were generated by irradiation of the AI/BMO photocatalyst with high-energy β particles. Fig. 1b shows the SEM image of the one−step hydrothermal synthesis of BMO. Fig, S1 shows the TEM images of BMO The inside of the yellow ellipse in the figure indicates the interior of the BMO hollow microsphere, and the outside of the ellipse is the shell of the BMO hollow microsphere. The SEM image of AI/BMO composite is shown in Fig, S2. The introduction of AI did not affect the morphology of BMO hollow microspheres. AI deposition had no effect on the morphology of BMO. Fig. 1c shows the SEM image of the Bi−Ag@BMO− 400 photocatalyst. The thickness of the photocatalyst nanosheet was thickened by the irradiation of the electron beam. Fig. 1d−g shows the elemental mapping of Bi, O, Mo, and Ag in Bi−Ag@BMO− 400, and it can be observed that Bi, O, and Mo are uniformly dispersed outside the BMO nanospheres. Ag is relatively evenly dispersed outside the BMO nanospheres, and more Ag exists at the opening of the nanospheres, which may lead to partial reduction of Ag^0 by β particles into the BMO nanospheres. Fig. 1h shows the TEM image of Bi−Ag@BMO− 400. As shown in the figure, there are more quantum dots at the boundary of the material. Fig. 1i − j is the HRTEM image of Bi−Ag@BMO− 400, which shows the gradual formation process of the lattice of Bi QDs. In Fig. 1i, the lattice spacing of 0.335 nm corresponds to the crystal plane (012) of Bi QDs. However, the lattice spacing of 0.327 nm and 0.331 nm is also the (012) crystal plane of Bi

QDs, but the lattice spacing is smaller than that of 0.335 nm. This may be because the (012) crystal faces of Bi QDs with a larger and more prominent lattice are irradiated for a longer time, and the (012) crystal faces of two Bi QDs with a smaller lattice spacing will also form a larger and more obvious lattice spacing after being irradiated for a longer time. Fig. 1j shows the existence of an Ag QD (111) crystal plane, which directly proves the existence of Bi/Ag double quantum dots.

The XRD patterns of the synthesized samples are shown in Fig. 2a. The diffraction peaks of Bi_2MoO_6 at 28.2°, 32.4°, 46.6°, and 55.4° in the sample are well matched with the (131), (200), (260), and (331) crystal planes of orthogonal BMO (JCPDS No.76 −2388). Typical XRD peaks with AIs of 23.6° and 39.2° belong to the diffraction peaks of the AI/BMO composite, which shows that AI was successfully introduced into BMO. The diffraction peaks of metallic bismuth in Bi@BMO and Bi−Ag@BMO− β composites are obvious and consistent with the standard card (JCPDS No. 85 −1329). In addition, the Bi−Ag@BMO− β composite showed feature peaks of BMO, and Bi QDs, and no impurity peaks were observed in the prepared material, indicating the successful synthesis of a high purity ternary crystal structure.

Fig. 2b shows the Raman spectra of BMO, Ag@BMO, Bi@BMO, AI/BMO, and Bi−Ag@BMO− 400. 146, 196, 288, 347, 799 and 845 cm^{-1} are characteristic Raman peaks of BMO. The irradiated samples exhibited Raman peaks similar to those of BMO in the range of
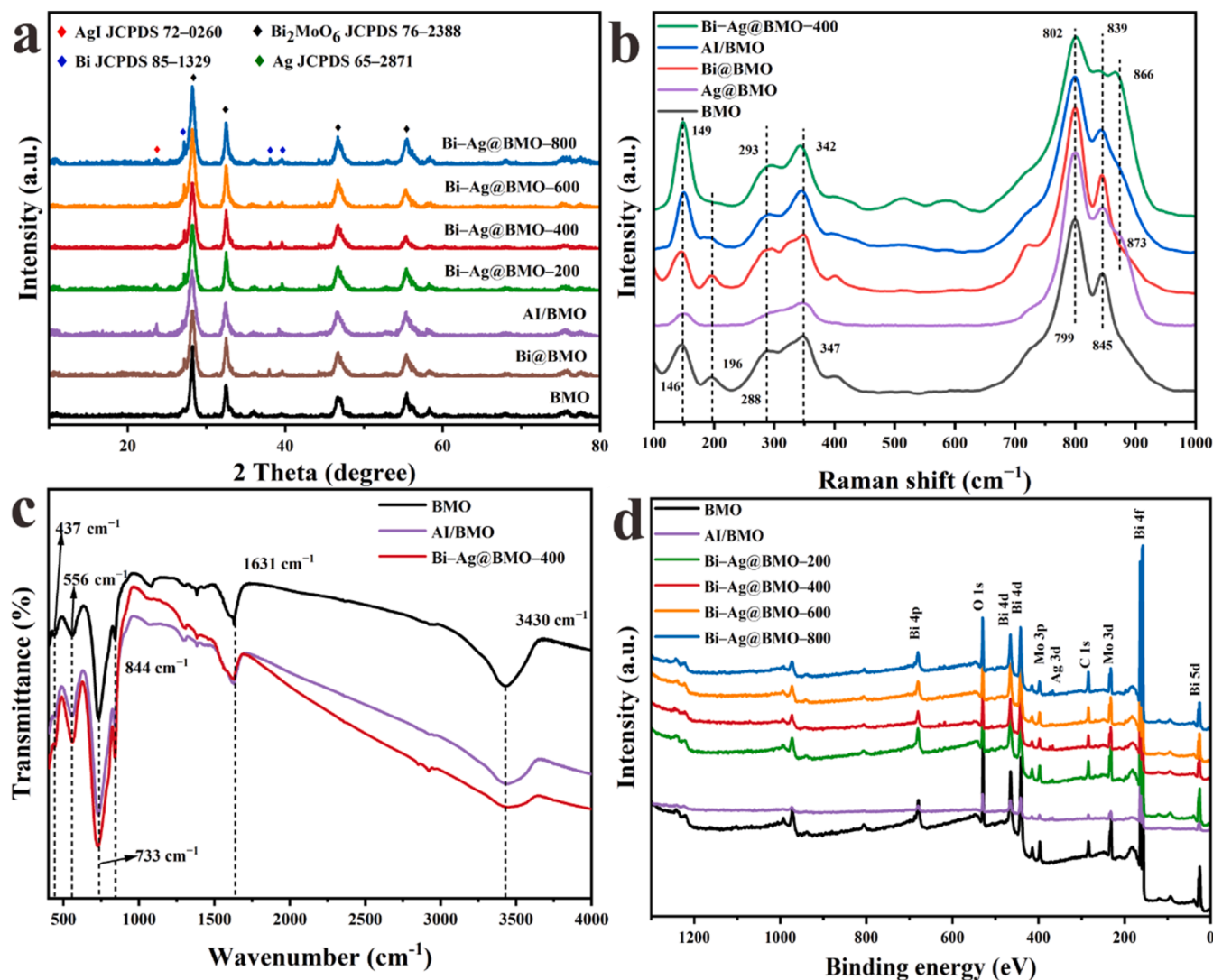

Fig. 2. (a) XRD patterns of the prepared samples. (b) Raman spectra of BMO, Bi@BMO, AI/BMO, Bi−Ag@BMO− 400. (c) FT-IR spectra of BMO, AI/BMO, Bi−Ag@BMO− 400. (d) XPS spectra of BMO, AI/BMO, Bi−Ag@BMO− 200, Bi−Ag@BMO− 400, Bi−Ag@BMO− 600, Bi−Ag@BMO− 800.

$100 - 1000\ cm^{-1}$, including vibration modes of Bi−O polyhedrons and MoO_6 octahedrons [25]. The Raman peaks of BMO in the $600 - 900$ and $200 - 400\ cm^{-1}$ ranges are directly related to the Mo−O bond length of the Mo−O stretching vibration band and the curved MoO_6 octahedron, respectively [26]. Compared with BMO, the Ag QDs@BMO composites showed almost no shift in the positions of the main Raman characteristic peaks in the vibrational modes of Bi−O polyhedra such as 146, 347, 799, 845 cm^{-1} and MoO_6 octahedra. The reduction in peak strength after loading AI may be related to AI coverage on the surface of BMO and the interaction between them. The above results combined with the Raman spectroscopy results of Bi QDs@BMO can demonstrate that the shift in the position of each Raman peak in Bi−Ag@BMO− 400 is mainly attributed to the formation of Bi−Ag DQDs [27]. The appearance of the Raman peak at 866 cm^{-1} may be due to the loading and formation of Ag QDs. In summary, by comparing the changes of Raman spectra after the introduction of Bi@BMO and Ag@BMO. It is clear that the synergistic introduction of Bi−Ag DQDs is the main reason for the shift of the Raman peak in Bi−Ag@BMO− 400.

As shown in Fig. 2c, the chemical bond and composition of the composite were tested by FT-IR. The characteristic peaks of the composite AI/BMO have similar characteristic peak signals to those of BMO, indicating the successful construction of AI/BMO composites. FTIR spectra of the material before and after β-particle irradiation show typical FTIR peaks belonging to BMO.The wide absorption band at 3430 cm^{-1} and 1631 cm^{-1} belong to the tensile vibration of O−H in adsorbed water [28]. The peaks from $1500 - 1000\ cm^{-1}$ are C−H bending vibration and C−O stretching vibration [29]. The absorption peaks at 844 cm^{-1} and 733 cm^{-1} belong to Mo−O and Mo−O−Mo bridges, respectively [30]. Both AI/BMO and Bi−Ag@BMO− 400 showed a significant enhancement of the characteristic peak signal at $437 - 844\ cm^{-1}$ compared to BMO.

The chemical composition and surface behavior of the photocatalysts were further investigated by XPS. The presence of Bi, O, Mo, and Ag on the Bi−Ag@BMO− β surface was verified by XPS measurement spectroscopy (Fig. 2d). As shown in Fig. 3, after the β-particle irradiation treatment, the Bi−O bond in the BMO molecule is broken by the β-particle, and the semi-bonded Bi^{3+} is more easily activated by the β-particle irradiation, which makes the binding energy of Bi^{3+} increase from 163.19 and 157.91 eV to 163.85 and 158.53 eV, which represents the decrease of this electron density. Characteristic peaks belonging to Bi^0 appear in the high-resolution XPS spectrum of Bi 4 f in Ag@BMO− 200, belonging to 162.85 and 157.45 eV, respectively, which represents an increase in electron density. The binding energy of Bi^{3+} increases and then decreases with the increase of β-particle

irradiation time. the binding energy of Bi^0 shows the same trend with the increase of β-particle irradiation time, and the peak area shows an increasing trend. This means that at irradiation doses below $200 - 600$ KGy, the Bi−O bond continues to break and Bi^0 is continuously generated. However, at an irradiation dose of 800 KGy, the binding energy of Bi^{3+} changes very little compared to that at 600 KGy and can be considered almost constant. This may be due to the fact that the effect of the electron beam on the composite decreases with increasing depth due to the steric effect. When the surface layer of Bi−O is exhausted by breaking, electron beam irradiation with higher energy and longer time is required to continue breaking the Bi−O bond. As the irradiation time increases, the size of Bi^0 may show a tendency to increase. The XPS of Ag is shown in Fig. 3b. The two strong peaks of AI/BMO near 367.46 and 373.57 eV are Ag $3d_{5/2}$ and Ag $3d_{3/2}$. The spectra of the irradiated samples can be further split into two peaks at 367.41 and 373.43 eV. Peaks at 367.91 and 373.89 eV can be assigned to Ag^0 species, clearly proving the presence of Ag^0 in Bi−Ag@BMO− β composites. These observations confirm that Ag^+ ions are successfully reduced to Ag QDs by β particle irradiation. It is noteworthy that the Bi 4 f and Ag 3d peaks of the sample are shifted toward the elevated binding energy after Bi−Ag double quantum dots loading. This change indicates that there exists a strong interfacial interaction between Bi−Ag double quantum dots and AI/BMO composites [31,32]. In general, the XPS of O 1 s can be decomposed into three peaks, which belong to chemisorption or dissociation of H_2O (O_C), oxygen vacancy (O_V), and lattice oxygen (O_L). As shown in Fig. 3c, Bi−Ag@BMO− β also showed oxygen vacancies after modification with β particles. The change in the Bi 4 f XPS spectrum is the increase or decrease in the binding energy of Bi^{3+} and the appearance of Bi^0, and the change in Ag 3d is the decrease in the binding energy of Ag^+ and the appearance of Ag^0, while the changes in O were more focused on the variation in the oxygen peak area. In addition, Bi^0 and O_V are often produced contemporaneously. Compared to the variations in Bi 4 f and O 1 s, the high-resolution Mo 3d XPS spectra have limited changes, and the chemical shifts are all within 0.10 eV. The composite of BMO irradiated and then induced with AgI was prepared and named as AI/Bi@BMO. its XPS spectrum is shown in Fig. S3. Probably due to the AgI loading, there is no very obvious Bi^0 characteristic peak in the spectrum of Bi 4 f.

The existence of quantum dots has an obvious influence on the optical responsiveness of the photocatalyst. UV−visible diffuse reflection spectroscopy was used to study the light absorption performance of the catalyst (Fig. 4a). BMO responds to light at wavelengths below 487 nm and has a redshifted absorption edge after loading Bi QDs or AI, which are 489 nm and 490 nm (Fig. S2), respectively. After β particle
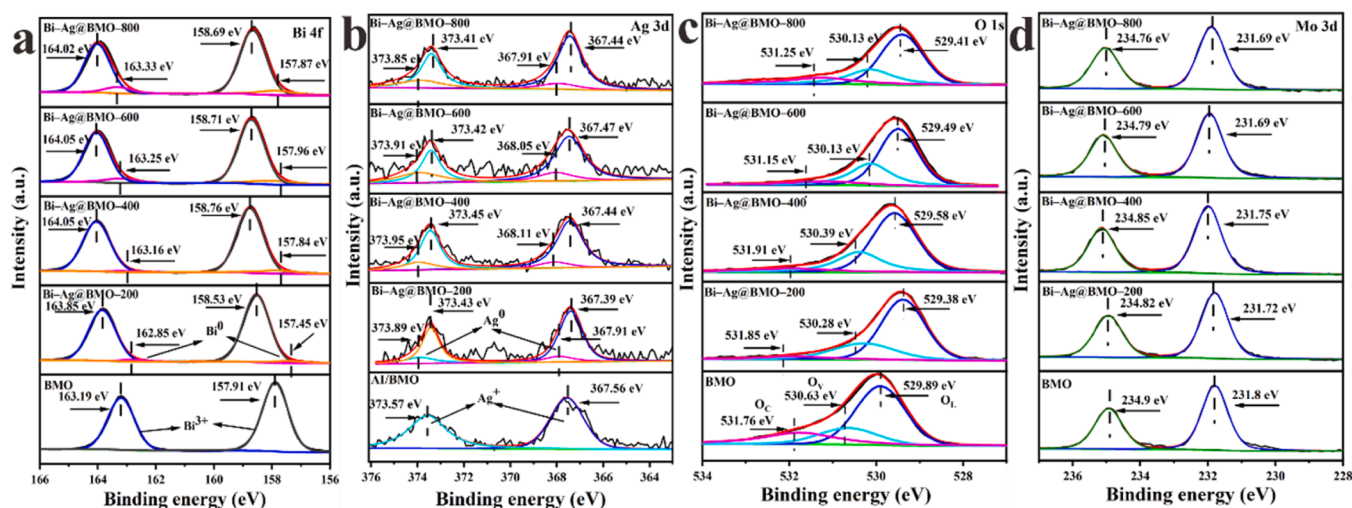

Fig. 3. XPS spectra of elements in BMO, AI/BMO, Bi−Ag@BMO− 200, Bi−Ag@BMO− 400, Bi−Ag@BMO− 600, and Bi−Ag@BMO− 800: (a) Bi 4 f; (b) Ag 3d; (c) O 1 s; (d) Mo 3d; (e) Elemental content of the sample surface.
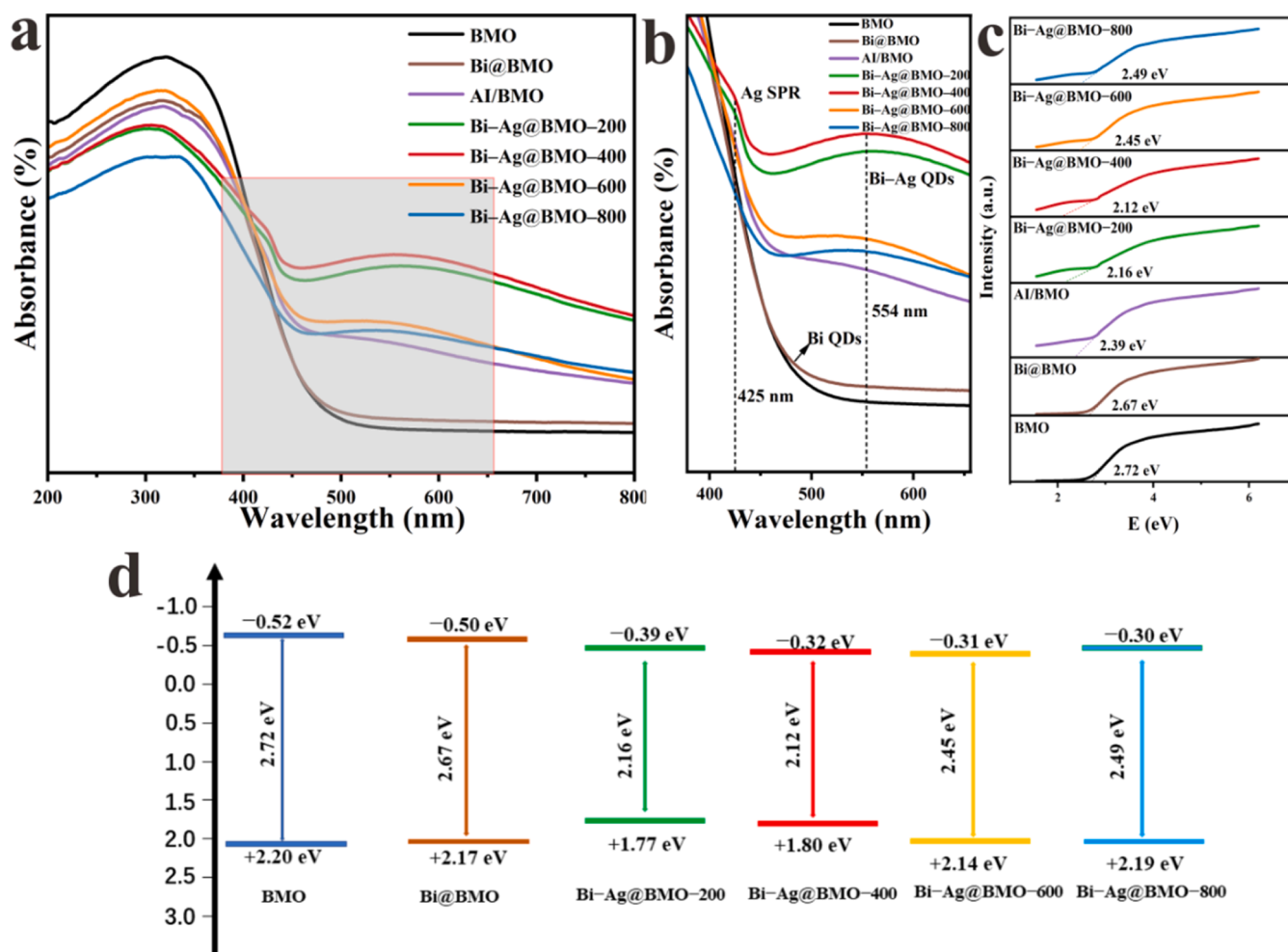
Fig. 4. (a−b) UV−visible absorption spectrum. (c) band gap. (d) Electrochemical Mott-Schottky plots. (e) Schematic illustration of the band structure of photocatalysts.

treatment, the absorption edges of Bi−Ag@BMO− 200, Bi−Ag@BMO− 400, Bi−Ag@BMO− 600, and Bi−Ag@BMO− 800 all show a great redshift, which may be caused by the SPR effect of Bi QDs. Fig. 4b shows the locally enlarged image of Fig. 4a at 450–650 nm. Bi−Ag@BMO− 200, Bi−Ag@BMO− 400, Bi−Ag@BMO− 600, and Bi−Ag@BMO− 800 materials have a peak at 425 nm. This is attributed to the SPR effect of Ag. Bi−Ag@BMO− β has a new peak at 554 nm compared with Bi@BMO. By comparing with much literature, we guessed that Ag QDs may enhance the SPR effect of Bi QDs, making the SPR peak of Bi QDs greatly increased [33–35]. Meanwhile, compared with Bi−Ag@BMO− 600 and Bi−Ag@BMO− 800, Bi−Ag@BMO− 200 and Bi−Ag@BMO− 400 have redshifted phenomena in the absorption of visible light, which may indicate that Bi QDs and Ag QDs have strong interactions [36]. The β particle induced lattice oxygen escape and the loss of negatively charged oxygen atoms led to the reapportionment of charge clouds within the lattice and the accumulation of free electrons on the surface of Bi QDs [15]. When the frequency of light is the same as the frequency of the conduction electrons of the metal, the nanometal strongly absorbs the incident light. The electrons after light absorption vibrate violently on the metal surface and cause a very strong electric field to be generated, which is the cause of surface plasmon resonance [37]. The energy band of the photocatalyst was calculated by the Kubelka-Munk equation through UV−vis diffuse reflection spectra (Eq. 1) (Eg):

$$\alpha h\nu = A(h\nu - Eg)^{n/2} \tag{1}$$

As shown in Fig. 4c, the Eg values of BMO, Bi@BMO, and AI/BMO are 2.72 eV, 2.67 eV, and 2.39 eV, respectively. After β particle irradiation, the energy band of Bi−Ag@BMO− 200, Bi−Ag@BMO− 400, Bi−Ag@BMO− 600, and Bi−Ag@BMO− 800 decreased to 2.16 eV, 2.12 eV, 2.45 eV, and 2.49 eV, respectively. The energy band of the Bi@BMO material is reduced by 0.05 eV compared with that of BMO. It can be seen that Bi quantum dots can slightly reduce the band gap of the composite and improve the absorption performance from visible light to near infrared light. Compared with the AI/BMO photocatalyst, the band gap of the Bi−Ag@BMO− 400 material decreases significantly by approximately 0.27 eV, indicating that the introduction of Ag QDs significantly changes the band gap value of the material and greatly improves the light absorption performance of the material from the visible light to near infrared light region.

To further investigate the effect of quantum dots on the energy band structure, a Mott-Schottky diagram of the composite was made. Since the M-S curve in Fig. S5 shows a positive slope, this indicates that the composite belongs to an n-type semiconductor. The flat band potential (E_{fb}) of the photocatalyst was determined by the M-S curve. The E_{fb} values of BMO, Bi@BMO, Bi−Ag@BMO− 200, Bi−Ag@BMO− 400, Bi−Ag@BMO− 600 and Bi−Ag@BMO− 800 are − 0.42, − 0.40, − 0.29, − 0.22, − 0.21, and − 0.20 eV vs. NHE, respectively. The E_{CB} potential of n-type semiconductors is generally considered to be negative by approximately − 0.1 eV compared to the E_{fb} potential [38]. BMO, Bi@BMO, Bi−Ag@BMO− 200, Bi−Ag@BMO− 400, Bi−Ag@BMO− 600, and Bi−Ag@BMO− 800 have conduction

potentials (E_{CB}) of -0.52, -0.50, -0.39, -0.32, -0.31, and -0.30 eV, respectively. The valence band potential (E_{VB}) is usually defined by Eq. 2:

$$E_g = E_{VB} - E_{CB} \qquad (2)$$

Therefore, the E_{VB} values of BMO, Bi@BMO, Bi−Ag@BMO− 200, Bi−Ag@BMO− 400, Bi−Ag@BMO− 600 and Bi−Ag@BMO− 800 are $+2.20$, $+2.17$, $+1.77$, $+1.80$, $+2.14$ and $+2.19$ eV, respectively. In addition, VB−XPS spectra were used to calculate the valence band potential of the composites, as shown in Fig. S6. BMO The E_{VB} values of Bi@BMO, AI/BMO, Bi−Ag@BMO− 200, Bi−Ag@BMO− 400, Bi−Ag@BMO− 600, and Bi−Ag@BMO− 800 are $+1.71$, $+1.62$, $+1.90$, $++1.79$, $+1.94$, $+1.80$ and $+2.07$ eV, respectively. There is no doubt that the E_{VB} values calculated with the VB−XPS spectra are more negative than those calculated with the M-S spectra and appear below the CB. It is possible that the quantum dots promote the creation of localized states, forming impurity energy level in the energy band, which is the cause of the abnormal position of VB [39]. The impurity energy level below the CB can trap the electrons generated from VB excitation and inhibit the recombination of photocarriers [40]. When light with energy greater than or equal to the energy gap is shone onto a semiconductor, the electrons in its VB will be excited and jump to the conduction band, leaving relatively stable holes in the valence band, thus forming an electron-hole pair. The presence of impurity level allows the material to absorb less energy than it would otherwise, meaning that photocatalysts may have better carrier density and photo utilization [23].

Band structure calculations show that BMO responds well to visible light at an appropriate band gap (2.72 eV). In addition, the VB potential of BMO (2.20 eV) was slightly higher than the standard redox potential of $OH^-/\cdot OH$ (1.99 eV vs. NHE), indicating that BMO was able to oxidize OH^- to $\cdot OH$. BMO also has a more negative CB potential (-0.52 eV) than the $O_2/\cdot O_2^-$ redox potential, and dissolved O_2 can be formed into $\cdot O_2^-$ [41].

Electrochemical impedance spectroscopy (EIS), photoluminescence spectroscopy (PL) and transient photocurrent response were used to analyze the effect of double quantum dots on the charge separation of the catalyst. EIS was used for measuring charge transfer resistance on solid surfaces or interfaces. The arc radius of EIS is proportional to the charge transfer resistance. Therefore, the smaller the arc radius is, the lower the charge transfer resistance and the easier the electron-hole pair separation. Compared with BMO, Bi@BMO has a smaller arc radius, which may be because the entry of Bi QDs reduces the interface charge transfer ability. The arc radius of Bi−Ag@BMO− 400 is the smallest, which may be due to the introduction of Ag QDs, which further reduces the resistance of interfacial charge transfer, thus enhancing the carrier migration ability. The transfer and migration of carriers and their capture rates in photocatalysts can be estimated by using photoluminescence (PL) emission spectra. Photoinduced carrier recombination leads to photoluminescent emission, which is usually proportional to the rate of carrier recombination [42]. BMO has a strong representative photoluminescence emission peak at 495 nm. The position of the peak is the same, but the intensity of the emission band decreases after the addition of Bi QDs, indicating that the introduction of Bi QDs inhibits the recombination of holes and electrons. After the addition of Ag QDs, the emission intensity of Ag QDs decreases further, and a new emission peak appears at 450 nm. Obviously, this indicates that Ag QDs can prolong the life of photogenerated carriers [43,44]. The time-resolved PL of the photocatalyst is shown in Fig. S7. The lowest PL intensity of Bi−Ag@BMO− 400 indicates that the recombination of photoexcited carriers (e^-/h^+) is low, and the addition of double quantum dots can significantly improve the photocatalytic performance. The transient photocurrent response of the photocarrier (e^-/h^+) is measured at the visible wavelength $\lambda > 420$ nm, and the transport dynamics of the photocarrier (e^-/h^+) are shown. The rapid increase in the initial photocurrent under light indicates that photocarriers are generated at the interface between the sample and electrolyte. After the peak photocurrent, it finally reaches equilibrium over time, showing great reproducibility and stability in more than 4 open and close cycles. To observe the relationship between the SPR effect of Bi QDs and that of Ag QDs, the transient photocurrent response was measured under the excitation of filters with different cutoff visible wavelengths (Fig. 5d). The results show that the photocurrent density decreases with wavelength shift.

3.2. Evaluation of the photodegradation performance of CIP

The change in CIP concentration (C/C_0) with time in different systems is shown in Fig. 6a. There was negligible degradation of CIP in dark conditions. In open light conditions, the concentration of CIP in different degradation systems decreased. The removal rate of 10.0 mg/L CIP by the photocatalyst was significantly increased after modification with β particles, Bi−Ag@BMO− 400 showed the most obvious improvement, and the removal rate of 10.0 mg/L CIP reached approximately 93.75% within 60 min. In the absence of light, the oxidation capacity of PMS is the main reason for changing the CIP degradation rate. Fig. 6c shows the curves of the photocatalytic degradation of CIP by the activation of different photocatalysts on PMS. The CIP oxidation efficiency of PMS is approximately 35.04%, and PMS greatly improves the catalytic performance of photocatalysts. When the PMS content was 0.075 mM, BMO, Bi@BMO, AI/BMO, Bi−Ag@BMO− 200, Bi−Ag@BMO− 400, Bi−Ag@BMO− 600, and Bi−Ag@BMO− 800 could degrade 38.05%, 52.58%, 73.83%, 98.95%, 100.0%, 94.54% and 91.60% CIP in 30 min, respectively. The pseudo first-order kinetic model was used to fit the photocatalytic degradation kinetics of ciprofloxacin in different catalytic systems. Fig. S8 shows that the pseudo first-order rate of the Bi−Ag@BMO− 400/PMS catalytic system is the highest, which is 5.40 times that of AI/BMO/PMS (Eq. 3). The above results showed that β particles greatly improved the activation of PMS by the photocatalyst. Through the analysis of Fig. 6a and Fig. 6c, it is not difficult to find that photocatalysts under different irradiation doses not only have different degradation effects on CIP but also have different activation effects on PMS. It has been proven that the particle size of Bi^0 increases with increasing irradiation dose [15,45], possibly because the Ag quantum dots are concealed by the gradually larger Bi QDs. At 600 KGy and 800 KGy doses, Ag absorption peaks could not be observed in the DRS spectra of the photocatalysts. This result can partially support the conjecture that Ag QDs are masked. Since Ag QDs are covered by Bi QDs, the SPR effect of Ag QDs is difficult to photoexcite. As a result, the performance of Bi−Ag@BMO− 600 and Bi−Ag@BMO− 800 photocatalysts is significantly different from that of Bi−Ag@BMO− 200 and Bi−Ag@BMO− 400.

$$-ln\,(C/C_0) = kt \qquad (3)$$

To further study the degradation effect of CIP in an actual water environment, by controlling the amount of Mg^{2+} to simulate the natural environment, the photocatalyst degradation effect of CIP in the presence of Mg^{2+} was studied. The presence of Mg^{2+} can inhibit the photocatalytic degradation of CIP to some extent (Fig. 7a). When Mg^{2+} exists in the solution, the CIP removal rate of Bi−Ag@BMO− 400 samples decreased from 93.75% to 85.08% at 60 min. This is due to the presence of Mg^{2+}, which consumes some OH^- and produces $Mg(OH)_2$, thereby reducing the total amount of $\cdot OH$ used in the catalytic process. Ca^{2+} had no significant inhibition of CIP degradation by the photocatalyst (Fig. 7b). Because of the difference in K_{sp}: $Mg(OH)_2$ (1.8×10^{-11}) $< K_{sp}$: $Ca(OH)_2$ (5.5×10^{-6}), this results in a much lower likelihood of Ca^{2+} binding to form $Ca(OH)_2$. In conclusion, the $\cdot OH$ radical is an active component that plays a role in the photocatalytic degradation of CIP. If there are cations in the water or system that can combine with OH^- to form corresponding precipitates, the photocatalytic degradation of CIP

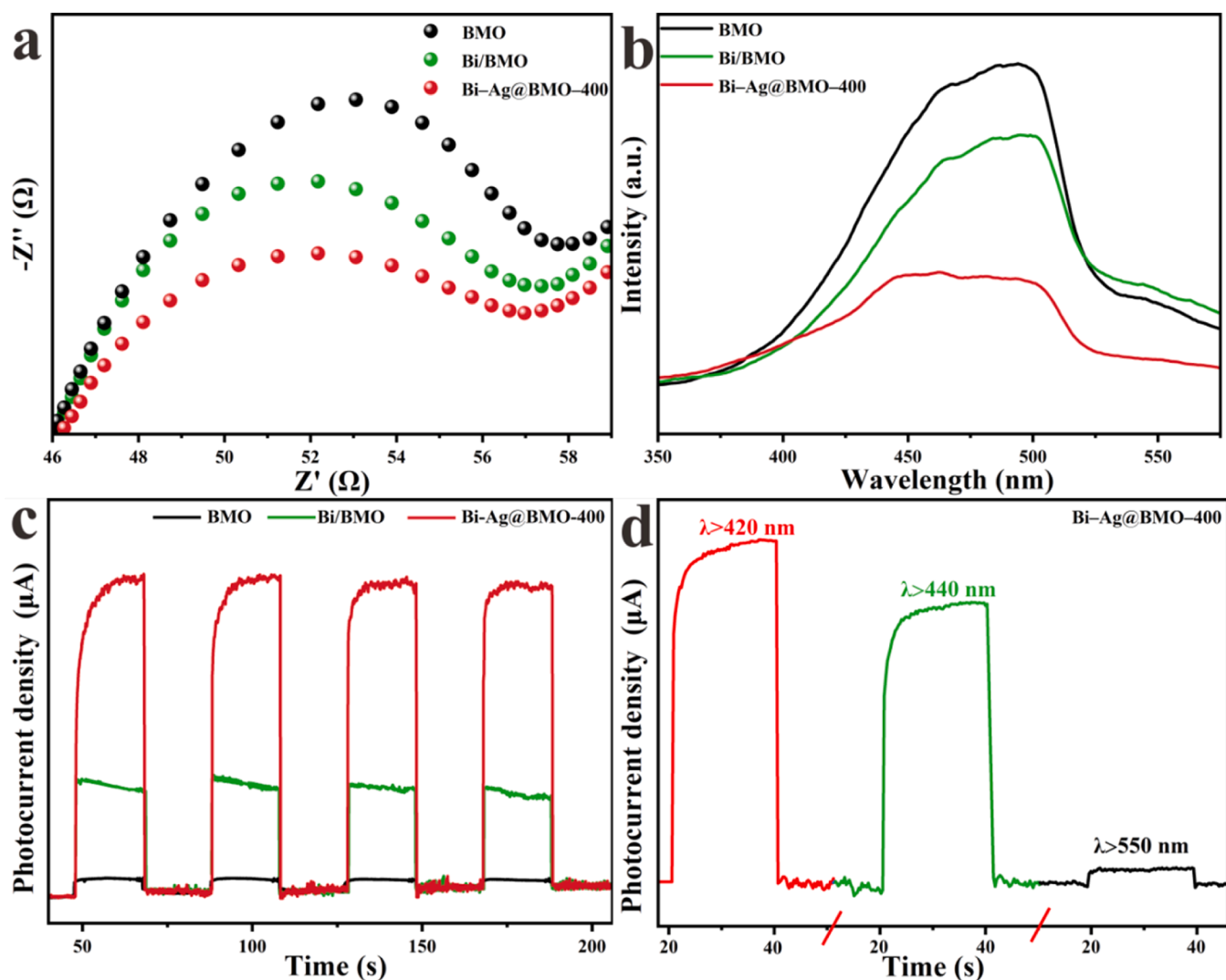**Fig. 5.** (a) EIS spectra. (b) PL spectra. (c) Transient photocurrent response of photocatalysts. (d) I-t response of Bi−Ag@BMO− 400 under different visible light cutoff filters ranging from 420 nm to 550 nm.

will be inhibited to a certain extent. In a CIP solution containing NO_3^-, the influence of NO_3^- on CIP degradation was studied. The presence of NO_3^- had no significant inhibitory influence on CIP degradation (Fig. 7c). These results indicate that the photocatalyst has good anti-interference ability for the photocatalytic degradation of CIP in natural water.

To investigate the degradation effect of the photocatalyst on CIP under various wavelengths of visible light irradiation, we used two wavelengths of visible light, 420–430 nm and 550–560 nm. The degradation of CIP by photocatalyst under visible light irradiation at wavelengths of 420–430 nm at 2 h: Bi−Ag@BMO− 400 was 79.13% for CIP removal at 10 mg/L (Fig. 7a), Bi−Ag@BMO− 200 was 72.63% for CIP removal at 10 mg/L, Bi−Ag@BMO− 600 for 10 mg/L was 55.54%, and Bi−Ag@BMO− 800 for 10 mg/L was 50.14%, while BMO and Bi@BMO showed 14.61% and 23.52% removal of CIP. As shown in Fig. 7b, the degradation of CIP by photocatalysts under visible light irradiation at wavelengths of 550–560 nm was 69.67% at 2 h for Bi−Ag@BMO− 400 at 10 mg/L. The degradation effect of other photocatalysts on CIP decreased to different degrees. This indicates that different irradiation doses have different effects on the formation and coupling of double quantum dots. The size of Bi QDs gradually increases with increasing irradiation dose [45]. Ag quantum dots hardly change with irradiation dose. As shown in Fig. 7c, under the combined irradiation of visible light

at 540–560 nm and 420–430 nm, the degradation effect of 10 mg/L CIP by the Bi−Ag@BMO− 400 photocatalyst was 97.21%, and the removal effect of 10 mg/L CIP by Bi−Ag@BMO− 200 was 89.77%. Bi−Ag@BMO− 600 showed 67.99% CIP removal at 10 mg/L, Bi−Ag@BMO− 800 showed 52.56% CIP removal at 10 mg/L, and BMO and Bi@BMO showed 16.01% and 25.27% CIP removal, respectively. The degradation of CIP by different photocatalysts at different wavelengths showed a huge difference. The enhancement of Bi−Ag@BMO− 400 was the most obvious when combining two wavelengths for irradiation. This was followed by Bi−Ag@BMO− 200, Bi−Ag@BMO− 600, and Bi−Ag@BMO− 800. $Bi_2 MoO_6$ and Bi@Bi_2. MoO_6 have almost no effect. Fig. 7d shows the photocatalysts used for the CIP degradation rate constant (k) at three wavelength conditions. After combining the two wavelengths, the k value of Bi−Ag@BMO− 400 is 0.03031 min^{-1}, which is 2.26 times the k value under 420–430 nm wavelength irradiation and 3.08 times the k value under 540–560 nm wavelength irradiation. This indicates that the photocatalytic effect of the material is enhanced under the combined irradiation of two wavelengths, and this enhancement may come from the fact that the SPR of Ag QDs is enhanced against that of Bi QDs when the Bi−Ag double quantum dots in the material are excited by visible light for the SPR effect. The best catalytic performance was obtained for Bi−Ag@BMO− 400 among the composites with different irradiation
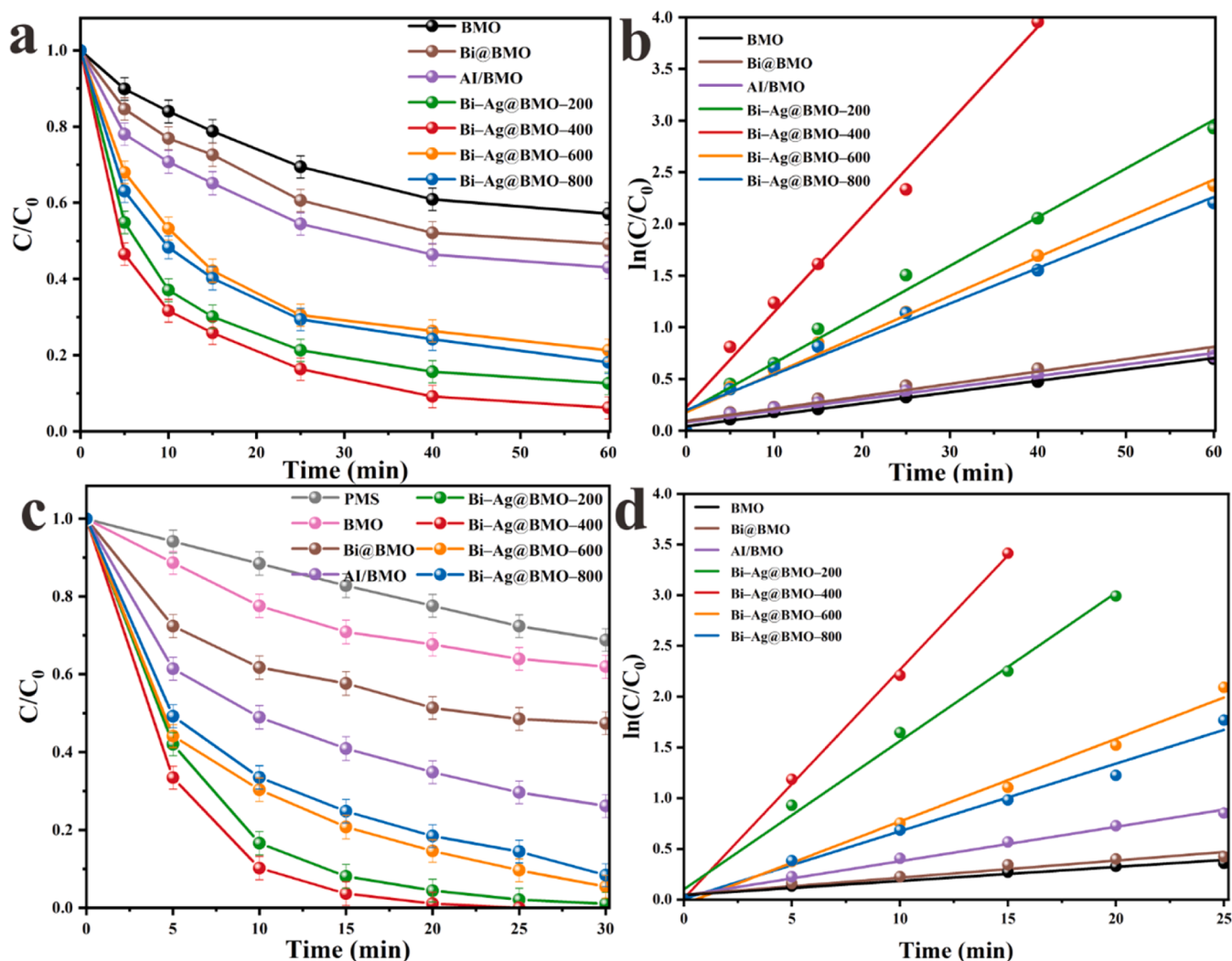
Fig. 6. (a, c) Degradation curves of CIP in different reaction systems. (b, d) Kinetic curves of CIP degradation in different reaction systems of CIP.

times. Also the response of Bi−Ag@BMO−400 was more pronounced for different wavelengths of light. This may be related to the Bi^0 size, which may affect the plasmon resonance effect between Bi−Ag DQDs.

The application potential of photocatalysts is very closely related to their commercial value of reusability. The reusability of Bi−Ag@BMO−400 was evaluated by cycling experiments under the same reaction conditions (Fig. S9). The catalyst still degraded 97.90% of the CIP after 5 replicate treatments. The XRD patterns of the photocatalysts before and after the cycling experiments were compared, and the components leading to the degradation of catalytic performance were investigated (Fig. S10). The XRD results show that the phase structure of the photocatalyst has not changed. The decrease in binding energy may be due to the atom gaining electrons, while the change in binding energy is related to the gain and loss of electrons [46]. In the analysis of the photocatalyst used to degrade CIP, a chemical shift of the O_V peak was found. The binding energy of O_V changes from 530.39 eV to 530.89 eV (Fig. S11c). The peaks of O_L, and Ag^0 show an increase in binding energy (Fig. S11c and b). The binding energy of Bi^{3+} in the Bi 4 f showed no obvious chemical shift before and after photocatalysis. The binding energy of Bi^0 decreased from 163.16 and 157.84 eV to 163.05 and 157.76 eV before and after photocatalysis. The decrease in binding energy represented the increase in electron density. The XPS map of Ag 3d showed that the binding energy of Ag^+ increased from 373.35 and 367.41 eV to 373.75 and 367.77 eV before and after photocatalysis, and the binding energy of Ag^0 increased from 374.11 and 368.11 eV to 374.

26 and 368.31 eV, the increase of binding energy represents the decrease of electron density. The increase of Ag^0 binding energy is in line with our expectation that good stability of Ag^0 can be maintained through the path of electron transfer. Double quantum dots are excited by light to form SPR effect, and hot electrons from double quantum dots enter the composite material. According to the change in binding energy, in the process of photocatalysis, hot electrons from Ag quantum dots may also enter Bi quantum dots, so the electron binding energy of Bi^0 increases. Because Bi QDs can trap electrons, they can absorb photogenerated electrons in the semiconductor, thus inhibiting the recombination of carriers [31] Fig. 8.

3.3. Mechanism of photocatalytic degradation of CIP

3.3.1. Active species analysis

For the determination of active free radicals produced by the oxidation reaction, EPR tests and free radical capture experiments were performed. In the Bi−Ag@BMO−400/Vis system, four characteristic peaks with an intensity ratio of DMPO·OH adducts of 1:2:2:1 can be observed at 5 min, as shown in Fig. 9a. In the Bi−Ag@BMO−400/PMS/Vis system, the DMPO·SO_4^- peak can be detected by adding PMS under the same conditions, and the concentration of·OH is increased. Obviously,·SO_4^- released by PMS after binding with e^- promotes the formation of·OH by oxidizing H_2O and OH^- [47]. Fig. 9b shows the signal characteristic peak belonging to·O_2^-. The Bi−Ag@BMO−400
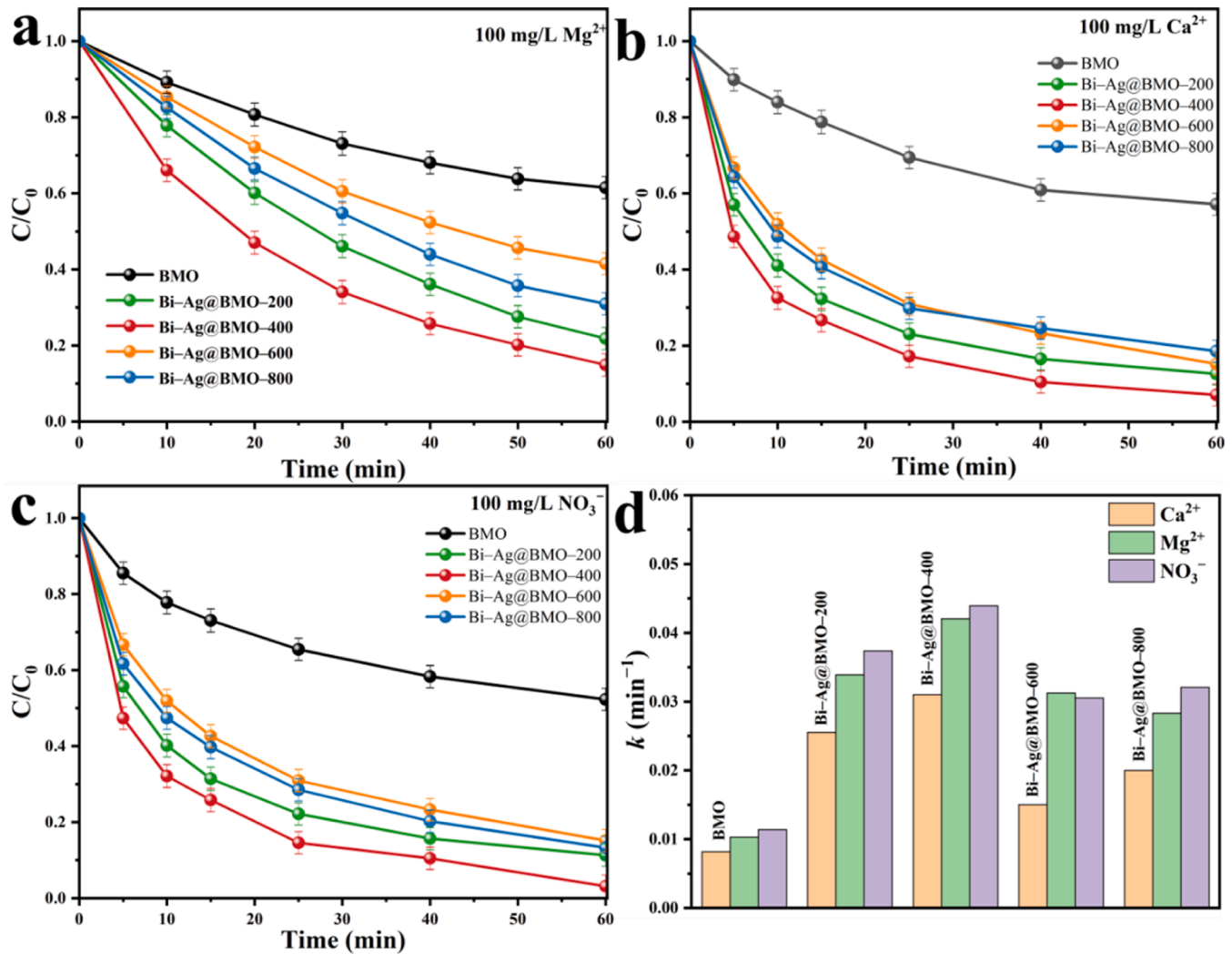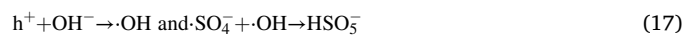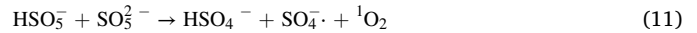
Fig. 7. Degradation curve (a, b, c) of ciprofloxacin under visible light for different photocatalysts in the presence of Ca^{2+}, Mg^{2+}, and NO_3^-; (d) rate constants (k) of CIP degradation.

composites can produce a certain intensity of $\cdot O_2^-$ under visible light. After the introduction of PMS, the signal peak of $\cdot O_2^-$ was greatly enhanced, while in the dark, no significant $\cdot O_2^-$ signal was detected. This indicates that $\cdot O_2^-$ is the dominant active species in the Bi−Ag@BMO− 400/PMS system. This result is consistent with the conclusion obtained from the free radical quenching experiment. Fig. 9c shows the attenuation of the TEMPO signal peak through EPR to observe the generation of h^+. The peak intensity of the Bi−Ag@BMO− 400/PMS/Vis system is slightly weaker than that of the Bi−Ag@BMO− 400/Vis system, indicating that the addition of PMS has no significant influence on the photolith holes. Fig. 9d shows the $^1O_2$ characteristic peak with an intensity of approximately 1:1:1. In the Bi−Ag@BMO− 400/Vis system, the characteristic signal peak intensity of $^1O_2$ does not change significantly under the conditions of light for 5 min and darkness. However, after the introduction of PMS, the characteristic signal peak strength of $^1O_2$ increases substantially, indicating that $^1O_2$ is mainly derived by the photolysis of PMS. These results suggest that $\cdot SO_4^-$, $\cdot OH$, $\cdot O_2^-$, and $^1O_2$ are reactive oxygen species (ROSs) that degrade antibiotic contaminants in Bi−Ag@BMO− 400/PMS/Vis system.

$$e^- + HSO_5^- \rightarrow \cdot SO_4^- + OH^- \tag{4}$$

$$h^+ + HSO_5^- \rightarrow SO_5^{2-} + H^+ \tag{5}$$

$$\cdot SO_4^- + OH^- \rightarrow SO_4^{2-} + \cdot OH \tag{6}$$

$$2\cdot SO_5^- \rightarrow 2\cdot SO_4^- + O_2 \tag{7}$$

$$e^- + O_2 \rightarrow \cdot O_2^- \tag{8}$$

$$H_2O + \cdot O_2^- \rightarrow \cdot OH \tag{9}$$

$$h^+ + OH^- \rightarrow \cdot OH \tag{10}$$

$$HSO_5^- + SO_5^{2-} \rightarrow HSO_4^- + SO_4^- \cdot + {}^1O_2 \tag{11}$$

$$\cdot O_2^- + h^+ \rightarrow {}^1O_2 \tag{12}$$

$$\cdot O_2^- + \cdot OH \rightarrow OH^- + {}^1O_2 \tag{13}$$

$$HSO_5^- + \cdot OH \rightarrow \cdot SO_5^- + H_2O \tag{14}$$

$$\cdot SO_4^- + \cdot SO_4^- \rightarrow S_2O_8^{2-} \tag{15}$$

$$\cdot SO_4^- + OH^- \rightarrow SO_4^{2-} + \cdot OH \tag{16}$$

$$h^+ + OH^- \rightarrow \cdot OH \text{ and} \cdot SO_4^- + \cdot OH \rightarrow HSO_5^- \tag{17}$$

3.3.2. Identification of reactive oxygen species

To further detect the main active substances involved in photocatalytic reactions, a series of quenching experiments were carried out
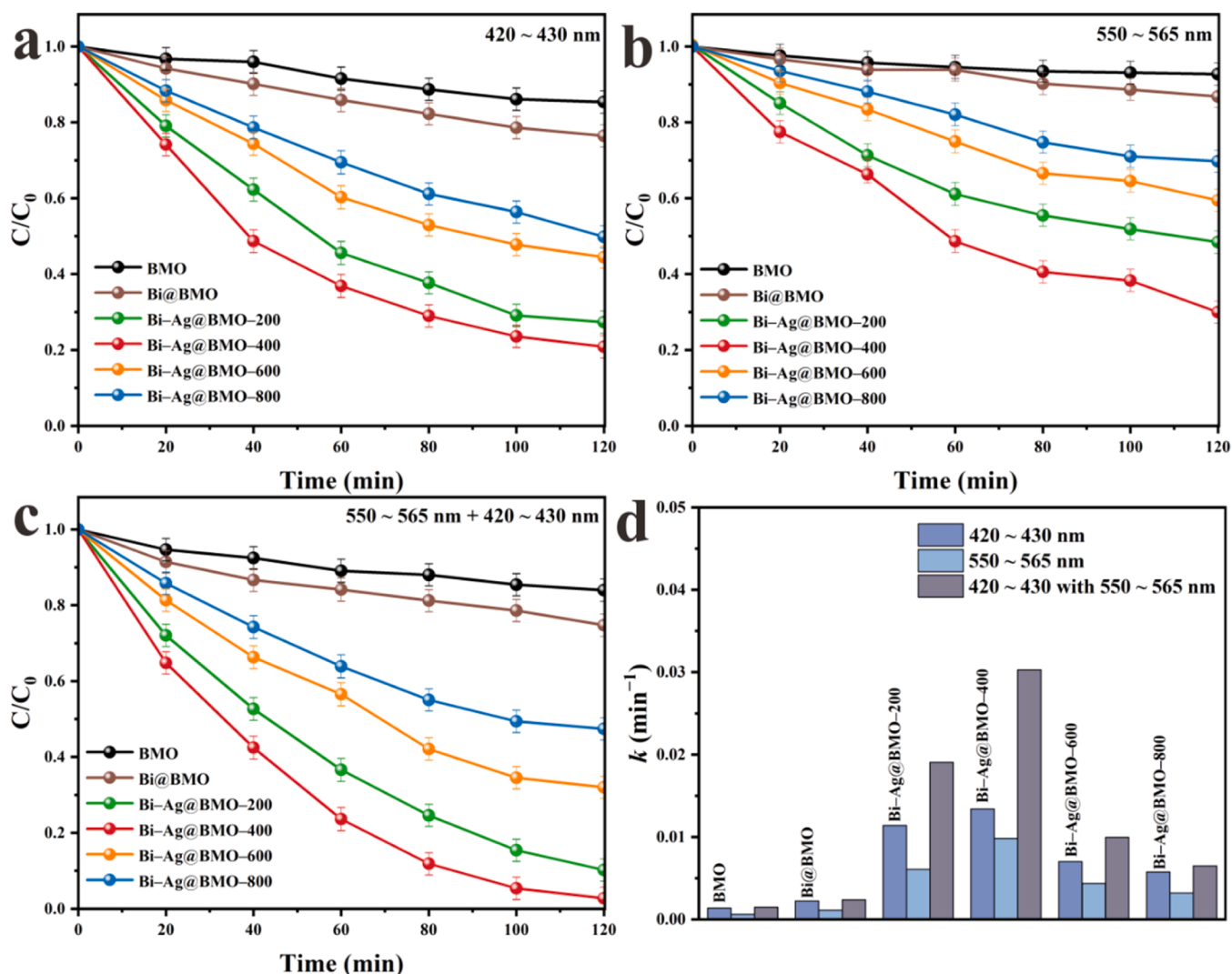
Fig. 8. (a−c) Degradation curves of CIP under different wavelengths of light irradiation. (d) Rate constants (k) of CIP degradation.

(Fig. S12). In this work, a series of scavengers, such as methanol (MeOH), tert-butanol (TBA), benzoquinone (BQ), disodium ethylenediamine tetraacetate (EDTA-2Na), dimethyl sulfoxide (DMSO) and L-histidine (His), were used to trap different free radicals. MeOH is considered a·OH ($k·OH=(1.2 −2.8) \times 10^9$ $M^{-1}·s^{-1}$) and·SO_4^- ($k·SO_4^-=(1.6 −7.7) \times 10^7$ $M^{-1}·s^{-1}$) capture agent, TBA is mostly considered a trapping agent of·OH ($k.OH=(3.8 −7.6) \times 10^8$ $M^{-1}·s^{-1}$). BQ is the trapping agent of·O_2^-, EDTA-2Na is the capturing agent of h^+, DMSO is the capturing agent of e^-, and L-histidine is the capturing agent of $^1O_2$. The control group cleared approximately 100.00% of CIP without a scavenger. After adding 50 mM TBA, the removal rate of ciprofloxacin was reduced from 100.00% to 71.40%. After adding 50 mM MeOH, the removal rate further decreased from 100.00% to 66.13%. Both·OH and·SO_4^- played a role in CIP degradation. The CIP degradation rate decreased from 100.00% to 23.45% after the introduction of 50 mM BQ, indicating that·O_2^- may be the main free radical in CIP degradation. When 50 mM EDTA-2Na and DMSO were added, the degradation rate of CIP decreased from 100.00% to 29.50% and 66.30%, respectively, indicating that h^+ had a greater effect on CIP degradation, while e^- played a certain role in CIP degradation. Finally, when 50 mM L-histidine was added, the CIP reduction rate was reduced to 19.44%. According to the above experimental results,·O_2^- and $^1O_2$ are the important active species of the photocatalytic reaction.

3.3.3. Degradation of ciprofloxacin by reaction parameters

By regulating the PMS dosage, oxygen concentration and pH value, the mechanism of the active ingredients on CIP degradation was explored. In the reaction, the CIP removal rate was determined by the release of·SO_4^-. The concentration of·SO_4^- free radicals is controlled by changing the initial content of PMS. After 25 min of illumination, Bi−Ag@BMO− 400 degraded only 35.34% CIP (Fig. S13). In the photocatalytic system supplemented with 0.013, 0.025, 0.050, 0.075, and 1.000 mM PMS, the removal rates of CIP within 20 min were 75.68%, 87.21%, 97.75%, 100.00%, and 100.00%, respectively. These results suggest that the introduction of more PMS can improve the degradation rate of CIP to some extent. However, with a further increase in PMS dosage, the degradation rate did not improve further [48]. There are two possible reasons for this: (1) The adsorption sites on the material for PMS are limited and too much PMS is not fully activated by the material [49]. (2) Excessive PMS may consume some of the free radicals, leading to a decrease in the reaction rate, and may also cause self-sudden extinction of·SO_4^- [10,47]. Therefore, the dosage of PMS was 0.075 mM in other experiments. The effect of H^+ and OH^- on the CIP removal rate was investigated by controlling the pH value of the liquid phase (Fig. S14). The results showed that photocatalytic degradation was inhibited in a highly acidic environment. Some researchers have found that when the solution is acidic, H_2SO_5 becomes the main component of PMS and remains stable in an acidic environment, thus inhibiting the activation of

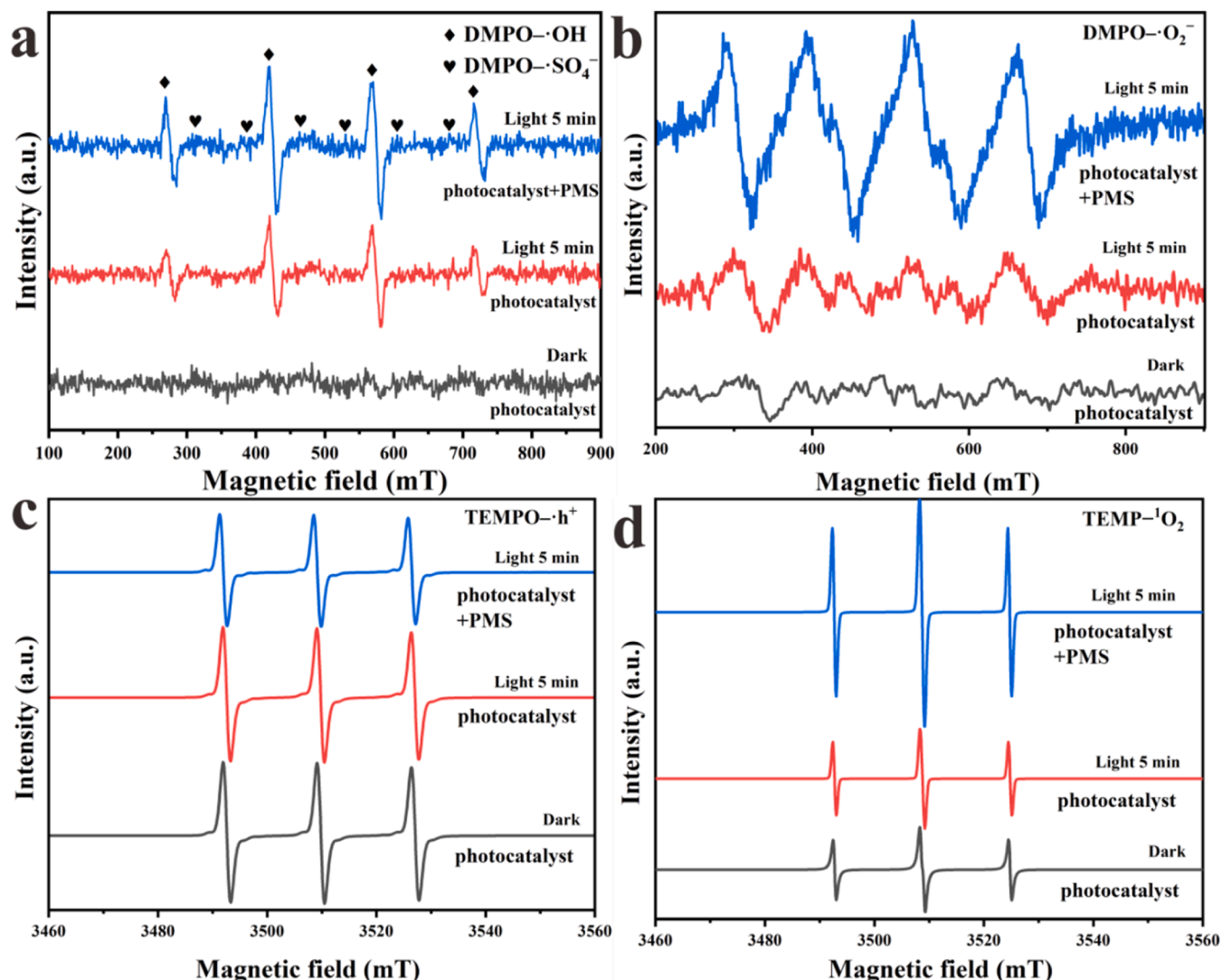**Fig. 9.** (a) DMPO-·OH and DMPO-·SO$_4^-$, (b) DMPO-·O$_2^-$ spin-tapping, (c) TEMPO-h$^+$ and (d) TEMP−^{1}O$_2$ ESR spectra in various processes.

PMS [50]. In addition, the increase in the pH of the solution is beneficial to the formation of hydroxyl groups, which can promote the activation of PMS [51]. However, too high pH can also inhibit the catalytic activity of the system. In a strongly alkaline environment, OH$^-$ consumes the·SO$_4^-$ radical (Eq. 16) to produce the weakly oxidized·OH. In addition, alkaline conditions promote the·OH release, and·SO$_4^-$ was consumed by excess·OH (Eq. 17), which reduced the removal rate of CIP. In conclusion, Bi−Ag@BMO− 400 can still maintain high activation performance for PMS over a wide pH range. As shown in Fig. S15, there is no significant change in CIP degradation after the presence of N$_2$ and O$_2$, indicating that dissolved O$_2$ plays a negligible role in the generation of·O$_2^-$. Usually, the conversion pathway of ^{1}O$_2$, including the autolytic decomposition of PMS[52,53], the reaction of PMS with some reactive groups (O−C═O, C═O, Fe−Nx, graphite N, etc.), and photoexcitation of oxygen molecules via the energy transfer pathway. And ^{1}O$_2$ is mainly derived from three species·O$_2^-$, dissolved oxygen and·SO$_5^-$[54]. As shown in Fig. S16, N$_2$ and O$_2$ atmospheres do not affect the removal efficiency of CIP, indicating that ^{1}O$_2$ is not generated by dissolved oxygen. Therefore, we propose that ^{1}O$_2$ is mainly generated by the direct decomposition of PMS on Bi−Ag@BMO− 400 from the·SO$_5^-$ radical. PMS adsorption on composites activated by electron transfer.

3.3.4. Possible degradation pathway for CIP

The main intermediates in the CIP degradation process were

analyzed by liquid chromatography—mass spectrometry (LC-MS), and the photocatalytic degradation pathway of CIP was revealed. In the Bi−Ag@BMO− 400/PMS system, three possible CIP photodegradation pathways were proposed (Fig. 10). In Pathway I, the cleavage and progressive oxidation of piperazine rings is an important mode. Pathway I begins with piperazine ring-opening to generate dialdehyde derivative P1 (*m/z* 362), then loses one formaldehyde to form P2 (*m/z* 334) or P2' (*m/z* 334), and then another formaldehyde is eliminated. This resulted in the formation of P3 (*m/z* 306). Subsequently, P3 (*m/z* 306) was transformed to P4 (*m/z* 291) after further oxidation and loss of amine nitrogen, and P4 (*m/z* 291) lost one formaldehyde to form P5 (*m/z* 263). Then, subsequent defluoridation converts P5 to P6 (*m/z* 245). The piperazine ring of CIP is completely destroyed, and the gradual opening of the piperazine ring is considered to be a common CIP oxidation pathway. This oxidation also occurs during ferrous persulfate activation and α-MnO$_2$-activated PMS [55]. CIP degradation Pathway II was consistent with that reported by Ahamad et al. [56].·OH radicals take part in the ring-opening reaction and hydroxyl substitution of quinolone rings and piperazines. The path reported by Yu et al. is similar to degradation Pathway III. [57]. P11 (*m/z* 348) is the product of electrophilic adduction and hydroxyl radical addition. After decarboxylation, hydroxylation, F substitution, and quinolone ring-opening, P13 is obtained. Finally, under the synergistic oxidation of·SO$_4^-$,·OH,·O$_2^-$ and ^{1}O$_2$, the ring-opening reaction occurs and eventually degrades into small

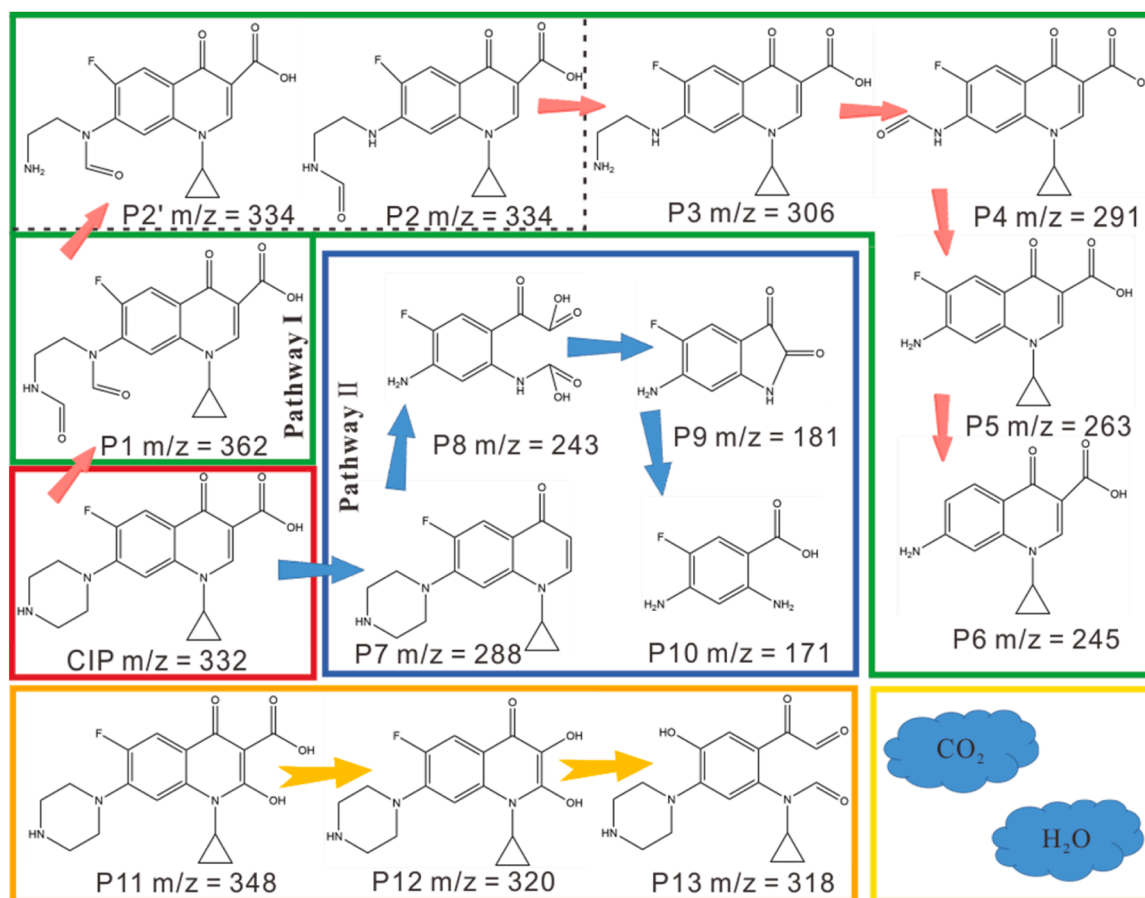**Fig. 10.** Possible degradation pathways of CIP by the Bi−Ag@BMO− 400 photocatalyst based on LC-MS.

inorganic molecules such as CO_2 and H_2O. Fig. S16 shows the secondary mass spectra and molecular formulas of the relevant products in Bi−Ag@BMO− 400/PMS degraded CIP solutions.

3.3.5. Charge differential density and first principle calculation

By calculating the differential charge density of each component of the whole composite, we can better understand the effect of each component on electron transfer. Fig. 11a shows the situation of electron transfer when the Ag−AI interface contacts and quantifies the whole system. The yellow electron cloud represents electron accumulation, and the blue electron cloud represents electron consumption. It can be seen that there is an electron transfer from AI to Ag QDs in Fig. 11a, which is approximately 0.035 electrons. Fig. 11b shows that AI will transfer 0.680 electrons to BMO when AI/BMO is formed, while Fig. 10c shows that Bi quantum dots will transfer 1.931 electrons to BMO when the Bi−BMO interface contract is formed. Compared with these quantified charge transfer amounts, we can obtain the electron transfer path during the gradual formation of the Bi−Ag@BMO− 400 system. When the AI/BMO heterojunction is formed, electrons will be transferred from AI to BMO driven by the built-in electric field, forming electron accumulation at the interface. After being irradiated by a high-energy electron beam, Bi−Ag double quantum dots are formed on the surface of the AI/BMO heterojunction. The work function of Bi QDs is approximately 4.22 eV, while that of BMO is approximately 6.52 eV [25]. The lower the work function is, the easier it is to transfer electrons, and the higher the work function is, the harder it is to transfer electrons, so there is Bi to BMO from low to high. At the same time, according to the number of transferred electrons, AI electrons tend to transfer to BMO rather than Ag QDs after the formation of the heterojunction.

The electronic structure and PMS adsorption activation mechanism of a series of transition metal single-atom catalysts were elucidated by DFT calculations. The first-principles analysis was used to simulate the adsorption of PMS on Bi/Ag double sites on Bi−Ag@BMO− 400 composite and the stepwise decomposition to form $^1O_2$, as shown in Fig. 11 (d-g). Firstly, as shown in Fig. 11d, one PMS molecule is adsorbed on each of the Bi/Ag dual sites on the Bi−Ag@BMO− 400 composite, and the S atom in the PMS molecule adsorbed on Bi is bonded to the O attached to the H atom in the PMS molecule adsorbed on Ag. In the second step, as shown in Fig. 11e, the PMS molecule adsorbed on the Bi/ Ag double sites is broken at an energy activation of 0.31 eV. The PMS molecule adsorbed on the Bi site breaks an O atom, and the PMS molecule adsorbed on the Ag site also breaks an O atom. The two broken O atoms are bonded to each other and bonded to Bi at the same time. In the third step, as shown in Fig. 11 f, the O−O adsorbed on Bi breaks with the Bi site to form $^1O_2$ at an energy of 0.53 eV.
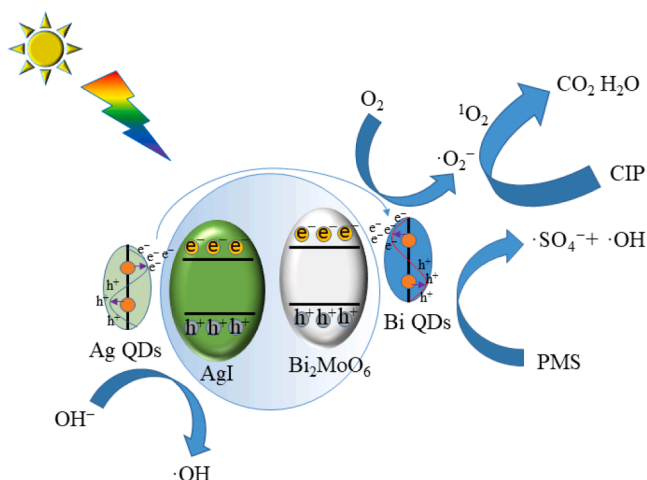
3.3.6. Photocatalytic mechanism

The possible mechanism of photocatalytic degradation of CIP by Bi−Ag@BMO− 400/PMS was proposed based on the previous characterization and experimental analysis. Under the excitation of visible light, the light-generated electron holes in the photocatalyst began to separate, as shown in Fig. 12. Electrons are photoexcited into the conduction band, while photogenic holes remain in the valence band. Electrons can break the O−O bond between PMS and dissolved oxygen, releasing·SO_4^- and forming hydroxyl radicals (·OH) through photogenic holes. At the same time, the Bi and Ag plasma effects on the surface of Bi−Ag@BMO− 400 are excited by incident light, thus generating hot electrons and hot holes. Some hot carriers may react with oxygen or water to form superoxide or hydroxyl radicals, respectively. Plasma hot electrons or holes can react directly with ciprofloxacin molecules or
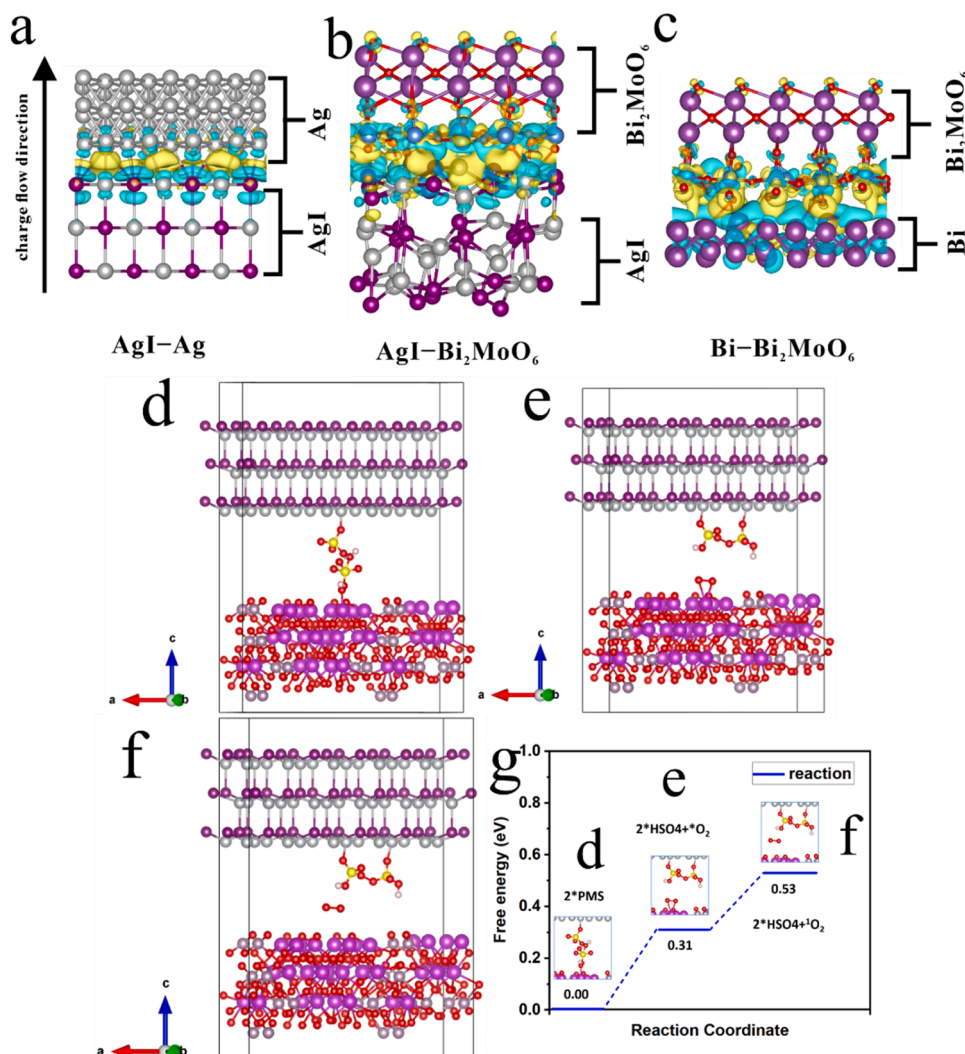
Fig. 11. (a−c) Charge difference distribution with charge accumulation in yellow and depletion in blue. (d) Modeling of PMS adsorption on Bi−Ag@BMO− 400, (e) Model of two PMS molecules breaking to form O−O, (f) Model for the formation of $^1O_2$ by O−O excitation of fracture formation, (g) Diagram of the change in energy of the reaction route.

Fig. 12. Possible photocatalytic mechanism.

indirectly degrade ciprofloxacin by activating PMS to form intermediate active species such as superoxide radicals ($\cdot O_2^-$) and singlet oxygen ($^1O_2$). At the same time, activation of persulfate by accepting electrons is more favorable than activation of O_2 because of the limited adsorption of O_2 [58]. With the synergistic oxidation of $\cdot SO_4^-, \cdot OH, \cdot O_2^-$ and $^1O_2$, a ring-opening reaction occurs and is eventually degraded into small inorganic molecules such as CO_2 and H_2O.

4. Conclusions

In summary, AI/BMO composite material was prepared by a two-step method, and Bi−Ag double quantum dots were successfully induced by β-particles. The formation of double quantum dots will greatly change the energy band structure, light absorption, carrier separation efficiency, accelerated electron transfer and so on. By activating PMS, Bi−Ag@BMO− 400 can degrade 10 mg/L CIP within 30 min and still shows good stability at pH 3–11 and in a simulated natural water environment. After 5 cycles, Bi−Ag@BMO− 400 can still maintain good performance and a stable structure. The introduction of Ag QDs is the key to the excellent photocatalytic activity of the material. First, a significant enhancement of the SPR effect of Bi QDs was successfully achieved through the coupling of Bi−Ag double quantum dots. Second, due to the lack of an effective PMS activation medium for BMO, it is only at

low concentrations that BMO can effectively degrade pollutants. Ag, as a noble metal, usually leads to complete activation of PMS and efficient degradation of CIP. The reactive oxygen quenching experiment and EPR experiment showed that the free radical mechanism dominated by $\cdot O_2^-$ and the nonfree radical mechanism participated by $^1O_2$ jointly promoted the degradation of CIP. This work is conducive to understanding the influence of quantum dots on the energy band structure and other aspects of materials, as well as further understanding the plasmon resonance effect of Bi and its use in practical applications.

CRediT authorship contribution statement

Yao Deng: Data curation, Investigation, Visualization, Writing – original draft preparation. **Juntao Wang**: Resources, Instrumental. **Jing Wang**: Resources, Investigation, Instrumental. **Huidi Zhang**: Data curation, Instrumental. **Hongbo Xiao**: Data curation, Investigation. **Cuihong Zhang**: Conceptualization, Resources, Instrumental. **Wenlei Wang**: Conceptualization, Funding acquisition, Supervision, Project administration, Writing – review & editing.

Declaration of Competing Interest

The authors declare that they have no known competing financial interests or personal relationships that could have appeared to influence the work reported in this paper.

Data Availability

No data was used for the research described in the article.

Appendix A. Supporting information

Supplementary data associated with this article can be found in the online version at doi:10.1016/j.apcatb.2023.123041.

References

[1] M. Qian, X.L. Wu, M. Lu, L. Huang, W. Li, H. Lin, J. Chen, S. Wang, X. Duan, Modulation of charge trapping by island−like single−atom cobalt catalyst for enhanced Photo−Fenton−Like reaction, Adv. Funct. Mater. (2023), 2208688, https://doi.org/10.1002/adfm.202208688.

[2] Y. Lin, C. Yang, Q. Niu, S. Luo, Interfacial charge transfer between silver phosphate and W_2N_3 induced by nitrogen vacancies enhances removal of β−lactam antibiotics, Adv. Funct. Mater. 32 (2021), 2108814, https://doi.org/10.1002/adfm.202108814.

[3] J. Yang, M. Zhang, M. Chen, Y. Zhou, M. Zhu, Oxygen vacancies in piezoelectric ZnO twin−mesocrystal to improve peroxymonosulfate utilization efficiency via piezo−activation for antibiotic ornidazole removal, Adv. Mater. (2023), 2209885, https://doi.org/10.1002/adma.202209885.

[4] T.-K. Kim, T. Kim, H. Park, I. Lee, A. Jo, K. Choi, K.-D. Zoh, Degradation of ciprofloxacin and inactivation of ciprofloxacin resistant E. faecium during UV−LED (275 nm)/chlorine process, Chem. Eng. J. 394 (2020), 124803, https://doi.org/10.1016/j.cej.2020.124803.

[5] P. Lu, K. Lin, J. Gan, Enhanced ozonation of ciprofloxacin in the presence of bromide: Kinetics, products, pathways, and toxicity, Water Res. 183 (2020), 116105, https://doi.org/10.1016/j.watres.2020.116105.

[6] L. Liu, K. Dai, J. Zhang, L. Li, Plasmonic Bi-enhanced ammoniated α-MnS/Bi_2MoO_6 S-scheme heterostructure for visible-light-driven CO_2 reduction, J. Colloid Interf. Sci. 604 (2021) 844–855, https://doi.org/10.1016/j.jcis.2021.07.064.

[7] F. Zhong, C. Yuan, Y. He, Y. Sun, J. Sheng, F. Dong, Dual-quantum-dots heterostructure with confined active interface for promoted photocatalytic NO abatement, J. Hazard. Mater. 438 (2022), 129463, https://doi.org/10.1016/j.jhazmat.2022.129463.

[8] M. Chen, J. Yao, Y. Huang, H. Gong, W. Chu, Enhanced photocatalytic degradation of ciprofloxacin over Bi_2O_3/$(BiO)_2CO_3$ heterojunctions: Efficiency, kinetics, pathways, mechanisms and toxicity evaluation, Chem. Eng. J. 334 (2018) 453–461, https://doi.org/10.1016/j.cej.2017.10.064.

[9] C. Liu, S. Mao, H. Wang, Y. Wu, F. Wang, M. Xia, Q. Chen, Peroxymonosulfate-assisted photocatalytic degradation performance of 2D/2D WO_3/BiOBr S-scheme heterojunction, Chem. Eng. J. 430 (2022), https://doi.org/10.1016/j.cej.2021.132806.

[10] G. Fang, T. Zhang, H. Cui, D.D. Dionysiou, C. Liu, J. Gao, Y. Wang, D. Zhou, Synergy between iron and selenide on $FeSe_2$(111) surface driving peroxymonosulfate activation for efficient degradation of pollutants, Environ. Sci. Technol. 54 (2020) 15489–15498, https://doi.org/10.1021/acs.est.0c06091.

[11] Y. Gao, Y. Zhu, T. Li, Z. Chen, Q. Jiang, Z. Zhao, X. Liang, C. Hu, Unraveling the high-activity origin of single-atom iron catalysts for organic pollutant oxidation via peroxymonosulfate activation, Environ. Sci. Technol. 55 (2021) 8318–8328, https://doi.org/10.1021/acs.est.1c01131.

[12] Y.D. Chen, R. Wang, X. Duan, S. Wang, N.Q. Ren, S.H. Ho, Production, properties, and catalytic applications of sludge derived biochar for environmental remediation, Water Res. 187 (2020), 116390, https://doi.org/10.1016/j.watres.2020.116390.

[13] X. Duan, H. Sun, S. Wang, Metal-free carbocatalysis in advanced oxidation reactions, Acc. Chem. Res. 51 (2018) 678–687, https://doi.org/10.1021/acs.accounts.7b00535.

[14] S. Shao, X. Li, Z. Gong, B. Fan, J. Hu, J. Peng, K. Lu, S. Gao, A new insight into the mechanism in Fe_3O_4@CuO/PMS system with low oxidant dosage, Chem. Eng. J. 438 (2022), 135474, https://doi.org/10.1016/j.cej.2022.135474.

[15] X. Hu, J. Wang, J. Wang, Y. Deng, H. Zhang, T. Xu, W. Wang, β particles induced directional inward migration of oxygen vacancies: Surface oxygen vacancies and interface oxygen vacancies synergistically activate PMS, Appl. Catal. B: Environ. 318 (2022), 121879, https://doi.org/10.1016/j.apcatb.2022.121879.

[16] M. Zhang, J. Ke, D. Xu, X. Zhang, H. Liu, Y. Wang, J. Yu, Construction of plasmonic Bi/Bismuth oxycarbonate/Zinc bismuth oxide ternary heterojunction for enhanced charge carrier separation and photocatalytic performances, J. Colloid Interf. Sci. 615 (2022) 663–673, https://doi.org/10.1016/j.jcis.2022.02.026.

[17] Z. Zhao, W. Zhang, X. Lv, Y. Sun, F. Dong, Y. Zhang, Noble metal-free Bi nanoparticles supported on TiO_2 with plasmon-enhanced visible light photocatalytic air purification, Environ. Sci.: Nano 3 (2016) 1306–1317, https://doi.org/10.1039/c6en00341a.

[18] X. Li, W. Zhang, W. Cui, Y. Sun, G. Jiang, Y. Zhang, H. Huang, F. Dong, Bismuth spheres assembled on graphene oxide: Directional charge transfer enhances plasmonic photocatalysis and in situ DRIFTS studies, Appl. Catal. B: Environ. 221 (2018) 482–489, https://doi.org/10.1016/j.apcatb.2017.09.046.

[19] K. Li, P. Chen, J. Li, Y. Sun, Y. Chu, F. Dong, Enhanced plasmonic photocatalytic disinfection on noble-metal-free bismuth nanospheres/graphene nanocomposites, Catal. Sci. Technol. 8 (2018) 4600–4603, https://doi.org/10.1039/c8cy01386a.

[20] Y. Yang, H. Chen, X. Zou, X.L. Shi, W.D. Liu, L. Feng, G. Suo, X. Hou, X. Ye, L. Zhang, C. Sun, H. Li, C. Wang, Z.G. Chen, Flexible carbon-fiber/semimetal Bi nanosheet arrays as separable and recyclable plasmonic photocatalysts and photoelectrocatalysts, ACS Appl. Mater. Interfaces 12 (2020) 24845–24854, https://doi.org/10.1021/acsami.0c05695.

[21] M. Plodinec, I. Grčić, M.G. Willinger, A. Hammud, X. Huang, I. Panžić, A. Gajović, Black TiO_2 nanotube arrays decorated with Ag nanoparticles for enhanced visible-light photocatalytic oxidation of salicylic acid, J. Alloy. Compd. 776 (2019) 883–896, https://doi.org/10.1016/j.jallcom.2018.10.248.

[22] R.S. Haider, S. Wang, Y. Gao, A.S. Malik, N. Ta, H. Li, B. Zeng, M. Dupuis, F. Fan, C. Li, Boosting photocatalytic water oxidation by surface plasmon resonance of Ag_xAu_{1-x} alloy nanoparticles, Nano Energy 87 (2021), 106189, https://doi.org/10.1016/j.nanoen.2021.106189.

[23] T. Kashyap, S. Biswas, S. Ahmed, D. Kalita, P. Nath, B. Choudhury, Plasmon activation versus plasmon quenching on the overall photocatalytic performance of Ag/Au bimetal decorated g-C_3N_4 nanosheets under selective photoexcitation: A mechanistic understanding with experiment and theory, Appl. Catal. B: Environ. 298 (2021), 120614, https://doi.org/10.1016/j.apcatb.2021.120614.

[24] M. Humayun, H. Ullah, Z.-E. Cheng, A.A. Tahir, W. Luo, C. Wang, Au surface plasmon resonance promoted charge transfer in Z-scheme system enables exceptional photocatalytic hydrogen evolution, Appl. Catal. B: Environ. 310 (2022), 121322, https://doi.org/10.1016/j.apcatb.2022.121322.

[25] X. Xu, L. Meng, J. Luo, M. Zhang, Y. Wang, Y. Dai, C. Sun, Z. Wang, S. Yang, H. He, S. Wang, Self-assembled ultrathin CoO/Bi quantum dots/defective Bi_2MoO_6 hollow Z-scheme heterojunction for visible light-driven degradation of diazinon in water matrix: Intermediate toxicity and photocatalytic mechanism, Appl. Catal. B: Environ. 293 (2021), 120231, https://doi.org/10.1016/j.apcatb.2021.120231.

[26] J. Ke, X. Duan, S. Luo, H. Zhang, H. Sun, J. Liu, M. Tade, S. Wang, UV-assisted construction of 3D hierarchical rGO/Bi_2MoO_6 composites for enhanced photocatalytic water oxidation, Chem. Eng. J. 313 (2017) 1447–1453, https://doi.org/10.1016/j.cej.2016.11.048.

[27] L. Zhang, Z. Wang, C. Hu, B. Shi, Enhanced photocatalytic performance by the synergy of Bi vacancies and Bi^0 in Bi^0-$Bi_{2-δ}MoO_6$, Appl. Catal. B: Environ. 257 (2019) 117785, https://doi.org/10.1016/j.apcatb.2019.117785.

[28] H. Zhou, J. Ke, H. Wu, J. Liu, D. Xu, X. Zou, Manganese tungstate/graphitic carbon nitride S-scheme heterojunction for boosting hydrogen evolution and mechanism exploration, Mater. Today Energy 23 (2022), 100918, https://doi.org/10.1016/j.mtener.2021.100918.

[29] G. Busca, A.S. Elmi, P. Forzatti, Mechanism of selective methanol oxidation over vanadium oxide-titanium oxide catalysts: a FT-IR and flow reactor study, J. Phys. Chem. 91 (2002) 5263–5269, https://doi.org/10.1021/j100304a026.

[30] Z. Yin, S. Qi, S. Deng, K. Xu, Z. Liu, M. Zhang, Z. Sun, Bi_2MoO_6/TiO_2 heterojunction modified with Ag quantum dots: a novel photocatalyst for the efficient degradation of tetracycline hydrochloride, J. Alloy. Compd. 888 (2021), 161582, https://doi.org/10.1016/j.jallcom.2021.161582.

[31] B. Wang, W. Feng, L. Zhang, Y. Zhang, X. Huang, Z. Fang, P. Liu, In situ construction of a novel Bi/CdS nanocomposite with enhanced visible light photocatalytic performance, Appl. Catal. B: Environ. 206 (2017) 510–519, https://doi.org/10.1016/j.apcatb.2017.01.047.

[32] K. Cheng, W. Sun, H.-Y. Jiang, J. Liu, J. Lin, Sonochemical deposition of Au nanoparticles on different facets-dominated anatase TiO_2 single crystals and resulting photocatalytic performance, J. Phys. Chem. C. 117 (2013) 14600–14607, https://doi.org/10.1021/jp403489r.

[33] F. Dong, Q. Li, Y. Sun, W.-K. Ho, Noble metal-like behavior of plasmonic Bi particles as a cocatalyst deposited on $(BiO)_2CO_3$ microspheres for efficient visible light photocatalysis, ACS Catal. 4 (2014) 4341–4350, https://doi.org/10.1021/cs501038q.

[34] F. Dong, Z. Zhao, Y. Sun, Y. Zhang, S. Yan, Z. Wu, An advanced semimetal-organic Bi spheres-g-C_3N_4 nanohybrid with SPR-enhanced visible-light photocatalytic performance for NO purification, Environ. Sci. Technol. 49 (2015) 12432–12440, https://doi.org/10.1021/acs.est.5b03758.

[35] Z. Zhao, W. Zhang, Y. Sun, J. Yu, Y. Zhang, H. Wang, F. Dong, Z. Wu, Bi cocatalyst/Bi_2MoO_6 microspheres nanohybrid with SPR-promoted visible-light photocatalysis, J. Phys. Chem. C. 120 (2016) 11889–11898, https://doi.org/10.1021/acs.jpcc.6b01188.

[36] B. Tudu, N. Nalajala, P. Saikia, C.S. Gopinath, Cu-Ni bimetal integrated TiO_2 thin film for enhanced solar hydrogen generation, Sol. RRL 4 (2020), 1900557, https://doi.org/10.1002/solr.201900557.

[37] Y. Li, M. Wen, Y. Wang, G. Tian, C. Wang, J. Zhao, Plasmonic hot electrons from oxygen vacancies for infrared light-driven catalytic CO_2 reduction on Bi_2O_{3-x}, Angew. Chem. Int. Ed. 60 (2021) 910–916, https://doi.org/10.1002/anie.202010156.

[38] L. Zhang, Y. Shi, Z. Wang, C. Hu, B. Shi, X. Cao, Porous β-Bi_2O_3 with multiple vacancy associates on highly exposed active {220} facets for enhanced photocatalytic activity, Appl. Catal. B: Environ. 265 (2020) 118563, https://doi.org/10.1016/j.apcatb.2019.118563.

[39] S. Bai, N. Zhang, C. Gao, Y. Xiong, Defect engineering in photocatalytic materials, Nano Energy 53 (2018) 296–336, https://doi.org/10.1016/j.nanoen.2018.08.058.

[40] R. Chen, Z. Ren, Y. Liang, G. Zhang, T. Dittrich, R. Liu, Y. Liu, Y. Zhao, S. Pang, H. An, C. Ni, P. Zhou, K. Han, F. Fan, C. Li, Spatiotemporal imaging of charge transfer in photocatalyst particles, Nature 610 (2022) 296–301, https://doi.org/10.1038/s41586-022-05183-1.

[41] H. Li, L. Jian, Y. Chen, G. Wang, J. Lyu, X. Dong, X. Liu, H. Ma, Fabricating $Bi_2MoO_6@Co_3O_4$ core-shell heterogeneous architectures with Z-scheme for superior photoelectrocatalytic water purification, Chem. Eng. J. 427 (2022), 131716, https://doi.org/10.1016/j.cej.2021.131716.

[42] Y. Qiu, F. Ouyang, R. Zhu, A facile nonaqueous route for preparing mixed-phase TiO_2 with high activity in photocatalytic hydrogen generation, Int. J. Hydrog. Energy 42 (2017) 11364–11371, https://doi.org/10.1016/j.ijhydene.2017.03.047.

[43] J.D. Xiao, L. Han, J. Luo, S.H. Yu, H.L. Jiang, Integration of plasmonic effects and schottky junctions into metal-organic framework composites: Steering charge flow for enhanced visible-light photocatalysis, Angew. Chem. Int. Ed. 57 (2018) 1103–1107, https://doi.org/10.1002/anie.201713194.

[44] D. Li, S.H. Yu, H.L. Jiang, From UV to near-infrared light-responsive metal-organic framework composites: Plasmon and upconversion enhanced photocatalysis, Adv. Mater. 30 (2018), 1707377, https://doi.org/10.1002/adma.201707377.

[45] J. Wang, W. Wang, J. Wang, K. Xue, Y. Peng, Y. Yan, Y. Wang, H. Wang, Y. Wu, The generation of lattice oxygen defects enhanced by β particles: Layered microsphere-like Bi_2WO_6 as a template leads to $Bi_x@Bi_{2-x}WO_n$ for the efficient removal of oxytetracycline, Chem. Eng. J. 416 (2021), 129197, https://doi.org/10.1016/j.cej.2021.129197.

[46] J. Tao, J. Yu, Q. Liu, G. Liu, H. Tang, Internal electric field induced S-scheme heterojunction MoS_2/CoAl LDH for enhanced photocatalytic hydrogen evolution, J. Colloid Interf. Sci. 585 (2021) 470–479, https://doi.org/10.1016/j.jcis.2020.10.028.

[47] Q. Li, G. Wei, L. Zhang, Z. Li, J. Li, Activation of peroxymonosulfate by a waste red mud-supported Co_3O_4 quantum dots under visible light for the degradation of levofloxacin, Chem. Eng. J. 452 (2023), 139382, https://doi.org/10.1016/j.cej.2022.139382.

[48] J. Yu, J. Zhang, T. Zeng, H. Wang, Y. Sun, L. Chen, S. Song, H. Shi, Stable incorporation of MnO_x quantum dots into N-doped hollow carbon: A synergistic peroxymonosulfate activator for enhanced removal of bisphenol A, Sep. Purif. Technol. 213 (2019) 264–275, https://doi.org/10.1016/j.seppur.2018.12.044.

[49] Y. Bu, H. Li, W. Yu, Y. Pan, L. Li, Y. Wang, L. Pu, J. Ding, G. Gao, B. Pan, Peroxydisulfate activation and singlet oxygen generation by oxygen vacancy for degradation of contaminants, Environ. Sci. Technol. 55 (2021) 2110–2120, https://doi.org/10.1021/acs.est.0c07274.

[50] H. Zhang, L.-c Nengzi, X. Li, Z. Wang, B. Li, L. Liu, X. Cheng, Construction of $CuBi_2O_4/MnO_2$ composite as Z-scheme photoactivator of peroxymonosulfate for degradation of antibiotics, Chem. Eng. J. 386 (2020), 124011, https://doi.org/10.1016/j.cej.2020.124011.

[51] M. Wang, Y. Tang, J. Wang, Z. Xu, Q. Dong, T. Ma, B. Lai, Promoted peroxydisulfate activation by nitrogen-doped carbon embedding iron on a nickel foam cathode: Performance, mechanism and relationship between C═O and $^1O_2$ generation, Chem. Eng. J. 460 (2023), 141638, https://doi.org/10.1016/j.cej.2023.141638.

[52] X. Duan, Z. Ao, H. Sun, S. Indrawirawan, Y. Wang, J. Kang, F. Liang, Z.H. Zhu, S. Wang, Nitrogen-doped graphene for generation and evolution of reactive radicals by metal-free catalysis, ACS Appl. Mater. Interfaces 7 (2015) 4169–4178, https://doi.org/10.1021/am508416n.

[53] J. Wang, S. Wang, Activation of persulfate (PS) and peroxymonosulfate (PMS) and application for the degradation of emerging contaminants, Chem. Eng. J. 334 (2018) 1502–1517, https://doi.org/10.1016/j.cej.2017.11.059.

[54] L.S. Zhang, X.H. Jiang, Z.A. Zhong, L. Tian, Q. Sun, Y.T. Cui, X. Lu, J.P. Zou, S.L. Luo, Carbon Nitride Supported High-Loading Fe Single-Atom Catalyst for Activation of Peroxymonosulfate to Generate $^1O_2$ with 100% Selectivity, Angew. Chem. Int. Ed. 60 (2021) 21751–21755, https://doi.org/10.1002/anie.202109488.

[55] J. Deng, Y. Ge, C. Tan, H. Wang, Q. Li, S. Zhou, K. Zhang, Degradation of ciprofloxacin using α-MnO_2 activated peroxymonosulfate process: Effect of water constituents, degradation intermediates and toxicity evaluation, Chem. Eng. J. 330 (2017) 1390–1400, https://doi.org/10.1016/j.cej.2017.07.137.

[56] T. Ahamad, M. Naushad, S.M. Alshehri, Analysis of degradation pathways and intermediates products for ciprofloxacin using a highly porous photocatalyst, Chem. Eng. J. 417 (2021) 127969, https://doi.org/10.1016/j.cej.2020.127969.

[57] H. Yu, J. Huang, J. Liang, X. Yuan, K. Yi, W. Zhang, J. Zhang, H. Chen, Steering photo-excitons towards active sites: Intensified substrates affinity and spatial charge separation for photocatalytic molecular oxygen activation and pollutant removal, Chem. Eng. J. 408 (2021) 127334, https://doi.org/10.1016/j.cej.2020.127334.

[58] S. Mandal, S.P. Nanavati, D.J. Willock, R. Ananthakrishnan, Band gap engineering of amine functionalized Ag(I)-based coordination polymers and their plasmonic Ag^0 coupled novel visible light driven photo-redox system for selective oxidation of benzyl alcohol, Appl. Catal. B: Environ. 303 (2022), 120821, https://doi.org/10.1016/j.apcatb.2021.120821.